MOF DERIVED HIERARCHICALLY POROUS NANOSTRUCTURES AS A ROBUST ELECTROCATALYST FOR EFFICIENT WATER OXIDATION.

By

Sroosh Tahir

Registration No.02182113024

Department of Physics
Quaid-i-Azam University
Islamabad, Pakistan

A dissertation submitted in partial fulfillment of the requirements for the degree of ***Master of Philosophy in Physics***

(2021-2023)

Declaration

I hereby declare that this thesis **"MOF derived hierarchically porous Nanostructures as a robust electrocatalyst for efficient water oxidation."** neither as a part nor as a whole, has been copied out from any source. It is further declared that the research work presented in this discussion has not been submitted for any other degree or qualification to any other university. If any part of this work is proven to be copied from any source, I, **Mrs. Sroosh Tahir** (Registration No.:02182113024), shall be legally responsible for punishment under the plagiarism rules of the Higher Education Commission (HEC), Pakistan.

Date: 12/12/2023

Signature of Student

Sroosh Tahir

Certification

I have carefully read and approved the thesis titled "**MOF derived hierarchically porous Nanostructures as a robust electrocatalyst for efficient water oxidation**." by Sroosh Tahir, Reg. no.02182113024. I recommend this thesis to the Department of Physics for acceptance, as it fulfills the requirements for the degree of Master of Philosophy in Physics.

Date: 12/12/2023

Research Supervisor

____

Dr. Naveed Zafar Ali
Experimental Physics Directorate,
National Centre for Physics (NCP),
Islamabad, Pakistan

Submitted through:

Head of Department

____

Dr. Kashif Sabih
Department of Physics,
Quaid-i-Azam University Islamabad,
Pakistan

Dedication

In heartfelt dedication to my grandmother (Fatam Jan), my parents (Tahir Hanif and Salma Khaliq), for their boundless love, endless sacrifices, heartfelt prayers and unwavering believe in my abilities. Your guidance and wisdom have been a constant source of inspiration, and I am forever grateful for the values you instilled in me

Acknowledgments

All glory belongs to **Allah**, the compassionate and the merciful. He is the origin of all knowledge. I express my utmost gratitude to the **Holy Prophet (peace be upon him)** who serves as a perpetual example of guidance and knowledge for all of mankind.

I express gratitude and humbleness to my esteemed supervisor **Dr. Naveed Zafar Ali** EPD Department, National Centre for Physics, Quaid-i-Azam University campus Islamabad for his superb guidance, support, and motivation during my M. Phil project. Thanks to his sincere and invaluable guidance and time. Your belief in my potential has make me able to successfully finish the task on time.

Most importantly, I am immensely grateful to my **parents,** my **grandmother** and **my brothers** for their intense support, benevolent blessings, and heartfelt prayers. To myself, I extend a heartfelt acknowledgement. This journey has been an odyssey of self-discovery resilience and self-belief. It is with a sense of pride and fulfillment that I recognize the effort invested in bringing this thesis to fruition.

Sroosh Tahir

Table of Contents

List of Figures

List of Tables

Abstract

Fossil fuels the predominant source of energy today, are a significant to the release of carbon dioxide into the atmosphere causing greenhouse effect and global warming. Alternative and renewable energy sources must be identified immediately in order to address these issues. Water, a readily available renewable energy resource, is an appealing option in this regard owing to its ability to produce H_2 (HER) and O_2 (OER) through water splitting mechanism. Utilizing distinct catalysts for the anodic and cathodic reactions in electrochemical water splitting reaction will escalate the cost of the electrolytic cell. Therefore, research and development efforts to develop novel electrocatalysts with dual functions for OER and HER is imperative and highly desirable. Metal Organic Framework (MOFs) and their derivatives are the well-known candidates having porous 3D -framework structures with high surface areas that have been rapidly developed in the last decade as an efficient electrocatalyst for water splitting. Among others, Zeolitic Imidazolate framework (ZIFs) are sub class of MOFs which have robust electrocatalytic properties are less explored for water splitting application. In this study we have prepared three different polymorphs of ZIF-7 porous framework material and their composite with zeolite both having sodalite topology. The three phases of ZIF-7 are described as ZIF-7-I, ZIF-7(I+III) and ZIF-7-III with a space group of rhombohedral(R-3), triclinic(P-1) and monoclinic(C2/c) respectively. ZIF-7 (I) is prepared from Zinc nitrate as metal nodes and benzimidazole as a linker, that crystallizes in the rhombohedral conformation with a lattice parameter of a=22.989[Å] b=22.989[Å] c=15.763[Å]. We further found that on addition of 1.25wt% of zeolite to pure ZIF-7(I) phase there triggers a phase transformation to ZIF(III) polymorph and we ended up into a combination of ZIF-7 (I+III) mixture. When the concentration of Zeolite increases to 5wt% into pure ZIF-7-I it is completely transformed into ZIF-7-III phase that crystallizes in the space group monoclinic (C2/c) with a lattice parameter of a= 16.106A b=19.511Å c=16.126Å. ZIF-7-I is further irradiated with 500 keV (Cu++) ions at dosages of 1 × 10^{14} ions cm^{-2}that causes yet another stimulating phase transformation from ZIF-7-I to a less symmetric ZIF-7-II polymorph that crystallizes in the space group triclinic (P-1) with a lattice parameter of a=23.984[Å] b=21.354[Å] c=16.349Å. All the synthesized materials were characterized utilizing XRD, FTIR, SEM, EDX, Raman spectroscopy, XPS, and TGA analysis. The crystallinity, phase purity and phase transformation from ZIF-7-I(rhombohedral) with a space group of R-3 to ZIF-7-III (monoclinic) with a space group of C2/c are confirmed by XRD. The average crystallite size of ZIF-7-I was found to be 15.687nm. The FTIR spectra of different polymorphs of ZIF-7 samples display the characteristics vibrational and stretching modes along with the formation of major bond at 426cm-1 attributed to Zn-N stretching modes that affirm the connectivity of metal nodes of Zn with benzimidazole linkers a vital part for the formation of porous framework. SEM images coupled with EDX revealed surface composition, morphology, and topography information of samples, confirming its crystallinity and phase purity and also tells the average particle size that was 61.5nm for pure ZIF-7-I. XPS for evaluation of elemental composition. The major elements that were present are C, N, O, $Zn2p_{1/2}$ and $Zn2p_{3/2}$ at binding energies of 285eV,399eV, 532eV, 1044eVand 1021eV respectively. Raman spectroscopy identify the major mode at 154cm^{-1} of Zn-Thermogravimetric Analysis for thermal stability evaluation reveals that ZIF-7-I was thermally stable up to 540 °C.

A suite of electrochemical techniques, including EIS to probe charge transfer resistance, LSV to determine the value of overpotential at 10 mAcm^{-2}, Tafel slope to determine the kinetics, and chronoamperometry to determine the material's stability. For ZIF-7(I+III) an overpotential of 290mV at 10mA cm^{-2} for the OER was reached. ZIF-7(I+III) electrocatalyst required only a cell voltage of 1.52V for water splitting and it performed very well among all catalysts. The high activity of ZIF-7(I+III) was further evidenced by a narrower semi-circle in Nyquist plot. Furthermore, higher stability was offered when tested with continual production of oxygen for 15 hours. The overpotential required for OER of pure ZIF-7-I was 414mV at 10 mAcm^{-2} with a Tafel slope of 66.98mV/dec and a wide semi-circle for EIS revealing good catalytic activity. The overpotential of combination of ZIF-7 (I+III) was 290mV with a Tafel slope of 59.21mV/dec and a small semi-circle for EIS showing the best catalytic activity. The overpotential for ZIF-7-III was 387mV with a Tafel slope of 48.49mV/dec and a wide semi-circle for EIS showing better catalytic activity. The comparative study of different polymorph both structurally and electrochemically shows that the best electrocatalyst for OER was the combination of two ZIF-7(I+III).

CHAPTER 1

1. INTRODUCTION

1.1 Sustainable Development & Energy Transitions a Path Towards Green Future

The rapid speed of industrialization and urbanization has fueled enormous economic growth, boosting the standard of living of trillions of people throughout the world. The biggest problem people face today is finding enough energy to maintain their standard of living. The population of the world currently uses 15 TW of electricity, and by 2050, that number is anticipated to increase to 30 TW. 85% of the energy used by humans today comes from fossil fuels, and their demand is anticipated to increase in the future [1].This development, however, has come at a high price, with rising emissions of greenhouse gases and ecological imbalances harming the environment and climatic stability. Although these resources are beneficial to mankind, but at the same time they are also harmful to humanity. Fossil fuels, are non-renewable and contribute to the net release of carbon dioxide (CO_2) into the environment, which is changing the global climate but, at the same time carbon dioxide can be used as a chance for extensive industrial-scale energy generation[2]. Recognizing the pressing need for a more comprehensive approach to development, the notion of sustainable development has emerged as a basic framework for addressing the intricate interplay of environmental, social, and economic concerns[3]. Developing countries are likely to play a critical role in the transformation of energy since they possess the majority of the leftover renewable energy and power consumption in these regions is expected to increase in the near future[4]. Because of the scale of these economies as well as their power systems, major adjustments may be implemented more quickly and easily than in developed countries[5]. The developed nations, like China, have progressed significantly in displacing the present fossil fuel-based power plants. The biggest solar plant on the sea was utilized for energy generation, along with other facilities for energy storage. It has a production capacity of 40 MJ. Japan also built the world's largest H_2 manufacturing facility that spans several kilometers, aiming to promote fuel cell technology and eliminate fossil fuel use. The chemical bond is crucial for energy and materials in the chemical industries worldwide. Storing renewable energy in chemical bonds and controlling it with storage and transmission methods is necessary. The sun, wind, water, and biomass can produce chemicals and electrical energy with ever-green solar energy [6]. The world needs 30 TW of energy by 2050, so sustainable energy and efficient storage are the only options to keep CO2 levels steady [7]. To achieve a sustainable future, we need to reduce costs and separate technology/infrastructure from energy/fuel production deadlines [8].

1.2 Water Splitting and Energy storage technology

By directly dissolving water into its component parts, the splitting of water is a technique for producing hydrogen and oxygen. Electrical (current), thermal (heat), and light (electromagnetic radiation) sources can all contribute to the energy needed to break a single H-O-H bond [9].

$$\mathbf{H_2O\ (l) \rightarrow H_2\ (g) + 1/2\ O_2\ (g)} \ldots\ldots\ldots\ldots\ldots \qquad \mathbf{(1.1)}$$

The volumetric co-production of oxygen equals half the volumetric co-production of hydrogen. The heat of reaction yields the entire energy demand of the reaction H, which can be partially met by heat (Q), while the remaining portion (change in Gibbs energy G) must be met electrically[10]:

$$\mathbf{\Delta H = \Delta G + \Delta Q} \ldots\ldots\ldots\ldots\ldots\ldots\ldots\ldots\ldots\ldots\ldots \mathbf{(1.2)}$$

In general, the difference in water splitting methods is formed anytime one or more types of energy source, such as electrolysis, thermolysis, or photolysis, is used to conduct the reaction. Electrolytic water splitting is fueled by flowing an electrical current through water, where electrical energy is converted to chemical energy takes place at the electrode-solution interface through charge transfer reactions in a unit called an electrolyzer [11] . The hydrogen and oxygen produced gas produced by water splitting can be stored for later use, making it an essential element of energy storage technologies.

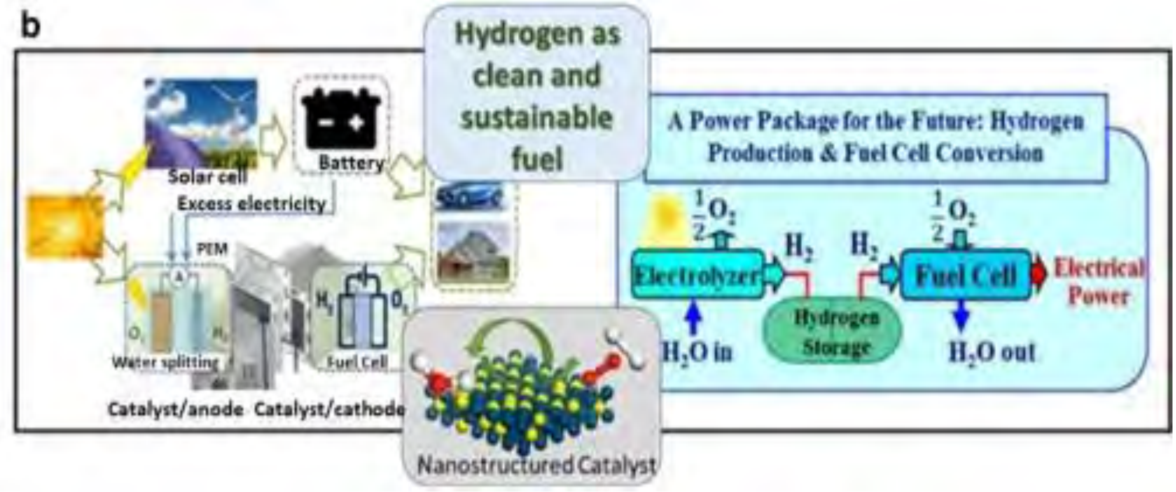

Figure 1.1: A sustainable power package with catalysis is highlighted in diagrams of a dual cell[12].

Electrolysis is more efficient and reliable for production of hydrogen and oxygen. In order to fulfill energy needs, different storage methods such as mechanical, thermal, and electric or chemical bonding are available[13].

Mechanical energy storage systems (MESSs) are very appealing because they have various benefits over conventional ESSs, particularly in terms of environmental effect, affordability, and sustainability. Mechanical energy storage systems (MESSs) are very appealing because they have various benefits over conventional ESSs, particularly in terms of environmental effect, affordability, and sustainability[14]. However, it can be used to make up for any power supply system failures when a significant amount of power is needed for a long-term objective. Solar thermal energy harnesses the sun's heat to convert water or small molecules to thermal energy [15]. Water that has been heated can be delivered to homes, building sites, and factories to enhance industrial processes using steam or vapor. If properly implemented, it is a simple solution that could take the place of natural gas. Using "batteries," or electrical storage devices, is another approach. Charging and discharging batteries creates electric potential through charged species building up on electrodes [16]. The electrodes' potential difference can be discharged with an external load. Li-ion batteries dominate the commercial energy storage market in portable electronics. More encouragingly, power can be stored using these energy storage technologies in conjunction with solar and wind energy.

Energy can also be kept in a similar way to how chemical bonds are kept together. According to this method, energy is stored in the form of organic interactions and can be released when needed by carefully breaking down chemical bonds. In this quest for the energy that permeates the entire planet, water is a particularly promising sources [17]. The building blocks of green protons, electrons, and oxygen molecules can be utilized for redox reactions and industrial compounds. Excitingly, H_2 molecules can be created from the generated protons, presenting a promising chemical solution for future energy demands. Various techniques for splitting water include thermal, thermochemical, and photo-biological methods. These methods have limitations such as high temperatures and low conversion efficiency. As a result, they are not as commercially viable. The key approach to solar-powered H_2 economy is now electrochemical and photo-electrochemical water splitting. To match current energy options, efficient electrolyzers must reduce costs considerably [18].

1.3. Role of electrocatalyst in water splitting

Water electrolysis involves two reactions: HER and OER, where H_2 and O_2 are formed at the cathode and anode respectively. The slow reaction dynamics caused by large overpotentials pose a challenge to practical water splitting. Highly efficient catalysts are needed to overcome this hurdle [19]. Electrocatalysts improve the productivity and kinetics of the water-splitting reaction, rendering it more practical and promotes the reactions while reducing overpotential[20].

Water splitting can be seen as

$2H_2O(l) \longrightarrow 2H_2(g) + O_2(g)$……………………………… (1.3

arises from a cathodic hydrogen evolution

$2H_2O + 2e^- \longrightarrow -2OH^- + H_2$…………………… (1.4)

$H^+ + e^- \longrightarrow -1/2H_2$…………………………………………… (1.5)

and anodic oxygen evolution reactions

$4OH^- - 4e^- \longrightarrow 2H_2O + O_2$………………… (1.6)

$H_2O - 2e \longrightarrow -1/2O_2 + 2H^+$………………… (1.7)

Here is the detailed explanation of the role of electrocatalyst in water splitting.

1.3.1 Reducing the energy barrier

Water electrolysis includes the anode oxidizing water molecules and the cathode reducing water molecules. However, in order for the reactions to occur, a significant amount of energy is often required to surpass the activation energy barrier. Electrocatalysts serve as catalysts, lowering the amount of triggering energy required for processes. They greatly increase the process's kinetics, rendering the water splitting procedure more efficient, by giving an alternate reaction route with lower energy barriers[21].

1.3.2 Enhancement of electron and proton transfer

Protons (H+) are discharged at the anode during water splitting, whereas electrons (e-) are created at the cathode. Electrocatalysts facilitate the effective transport of both electrons and protons to and from reaction sites, guaranteeing a constant flow of charges while minimizing energy losses. They serve as mediators, transporting protons as well as electrons between reactants and reaction sites, increasing the electrolysis process's overall efficiency[22].

1.3.3 Ensuring precision and Durability

During water splitting, electrocatalysts are intended to be selective for certain reactions, such as the oxygen evolution reaction (OER) on the anode and the hydrogen evolution reaction (HER) on the cathode. They reduce undesirable side reactions that might cost energy or cause the catalyst to degrade. Furthermore, electrocatalysts must be robust under difficult water splitting circumstances like high temperatures along with acidic or alkaline environment. Stable electrocatalysts enhance the water splitting process's endurance and dependability[23].

1.3.4 Dual-Function or Tandem Electrocatalysts:

Dual or dual-functional electrocatalysts have been created to speed up both the anodic and cathodic processes at the same time, enhancing water splitting efficiency even more. These catalysts are intended to feature both OER and HER active sites, enabling improved charge transfer and quicker reaction rates[24].

1.4 Catalysts for HER and OER

Bifunctional catalysts for the Hydrogen Evolution Reaction (HER) plus Oxygen Evolution Reaction (OER) are electrocatalytic materials which can promote both hydrogen gas synthesis and oxygen gas creation at the same time. These catalysts are essential in a variety of renewable energy technologies, including water electrolysis, which includes the separation of water into its basic elements, hydrogen and oxygen[25].

Ir, Ru and their oxides are preferred in the OER process due to slow kinetics and multistep proton-electron transfer. Noble metals are great catalysts in HER and ORR. Their capacity to reduce overpotential and improve reaction kinetics adds to excellent energy conversion efficiency. Noble metals are well-known for their durability and resilience under extreme electrochemical conditions, which makes them ideal for long-term use in devices such as fuel cells as well as water electrolyzers. The fundamental disadvantage of noble metal-based electrocatalysts includes their high cost and scarcity, particularly for metals such as platinum and iridium. This pricing barrier may stymie large-scale commercial uses of noble metal-only technology[26]. There is an urgent need to create non-noble-metal-based electrodes in order to cut catalyst prices and cope with the problem of declining valuable metal reserves in the future. Non-noble transition metal-based catalysts are a more cost-effective alternative with encouraging performance, making them key prospects for furthering sustainable energy systems. Continuous research is being conducted to improve the effectiveness and long-term reliability of non-noble metal-based catalysts in order to speed their incorporation into diverse energy conversion and storage system[27].

Non-precious metal catalysts are usually made of LDHs and transition metals like phosphides, sulphides, and selenides. Meanwhile, Pt and its alloys with Pd, Cu, and Co are still the best catalysts for the HER process [28]. Using a variety of catalysts during electrochemical water division can be costly and may lead to contamination of the counter electrode, reducing its effectiveness; therefore, non-precious-metal-based materials like transition metal phosphides, sulphides, and selenides are a better option due to their high HER performance [29].16,17 As a result, research and development of dual-function electrocatalysts to support OER and HER is both important and desired. The related design would be designed based on numerous factors, such as appropriate dimensions and shape, advantageous conductivity, the presence of a hierarchical porous framework and a large number of accessible active sites, and so on[30][31].

1.5 MOF based materials for potential electrocatalyst

Porous/Permeable materials are of incredible logical and mechanical interest because of their important applications in particle trade, sorption, division, sand catalysis. Depending on the size of the pores they contain, these solids are categorized as microporous, mesoporous, and macroporous. Microporous solids are those with pores that are 2 nm or smaller in size. Mesoporous solids have pores with a size range of 2 nm to 50 nm, whereas macroporous materials are those with pores larger than 50 nm [32]. Enacted carbons (ACs), zeolites, Zeotypes, Metal Organic Framework (MOFs) covalent natural systems (COFs), and certain polymers are instances of microporous solids.

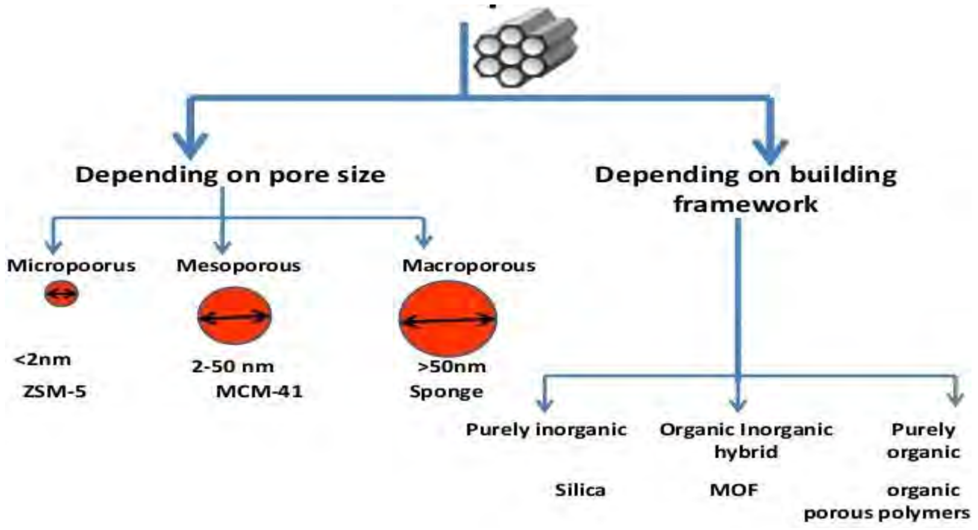

Figure 1.2: Depicts classification of porous materials[33]

MOFs are a kind of coordination polymer that has cavities or channels formed by the repeating of coordination units in one, two, and three dimensions. They are architecturally varied materials with organic (organic ligands) and inorganic (metal ions, metal nodes, metal groups) components connected by covalent connections to create a crystalline repetitive cage like framework[34].Metal nodes and metal clusters are typically made up of transition metals with vacant d-orbitals. As a result, they function as Lewis's acids, receiving electrons from organic linkers to create coordination[35].

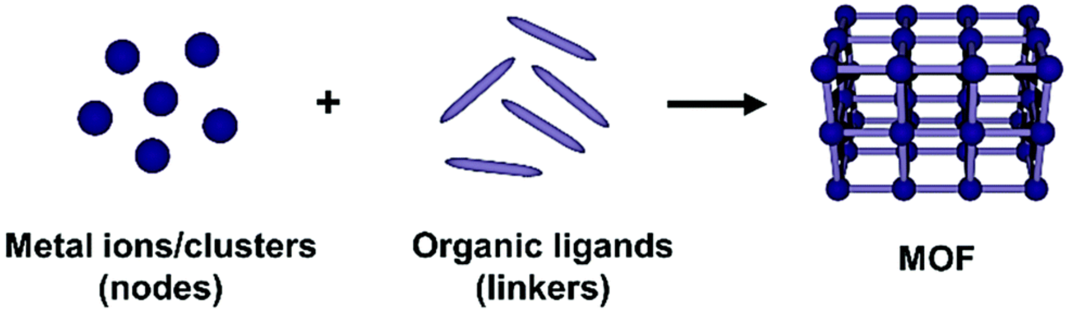

Figure 1.3: 3D MOF structure[115]

MOFs are crystal materials with high porosity and surface areas exceeding 6000 m2/g. They have potential uses in clean energy, as storage media for gases and high-capacity adsorbents. MOFs add to the diversity of their structures and have various applications, including thin-film tech and catalysis. They blend organic and inorganic chemistry beautifully [36]. Metal-organic frameworks have vast internal surface areas and adjustable properties. The article "Metal-organic framework functionalization and design strategies for advanced electrochemical energy storage devices" discusses strategies for energy storage using MOFs. MOF-based materials have proven to be highly preferable to other porous substances as electrocatalysts for OER due to their outstanding characteristics. The coupling of porous passages in MOFs having accessible locations with redox ability may allow for greater active site utilization efficiency than standard heterogeneous catalysts. However, their electrocatalytic uses are severely limited because to poor electrical conductivity as well as poor chemical stability[37]. When additional porous materials are incorporated into MOFs or Integrating MOFs with sophisticated functional materials such as nanocarbons and inorganic nanoparticles (NPs) is an effective way their pore size surface area and active site increases to achieve the exceptional electrocatalytic performance. This makes MOFs attractive options for applications requiring enhanced performance, such as fuel cells, water splitting, and the removal of contaminants [38].

1.6 A brief history of MOFs

MOFs may be traced back to 1706, when the Prussian blue pigment was synthesized. In this pigment, Fe2+ and Fe 3+ are linked by cyanide (CN)ligands to create a three-dimensional polymeric network with a cubic structure, which is characteristic of coordination polymers (Figure 1.14)[39].The perfect alignment of materials inspired scientists to create comparable materials with better characteristics.

Until the year 1990, numerous materials exhibiting tetrahedral and octahedrally connected structures were suggested by Robons [40]. These materials possessed potential features including elevated crystallinity, thermal and mechanical stability, as well as functional pores conducive to guest molecule diffusion and catalytic sites amenable to heterogeneous catalysis and cooperative functionalities.

In the year 1999, Omar Yaghi, who is credited with coining the term "metal-organic framework," synthesized MOF5 by reacting zinc nitrate with terephthalic acid benzene dicarboxylic acid (BDC) (as shown in Figure 1.4)[41]. MOF-5, which has a cubic network structure similar to that of Prussian blue, aroused great excitement due to its permanent porosity after guest molecule removal. Additionally, it demonstrated the highest BET surface area ever recorded (2900m2 /g with pore volume 1.04cm3 /g) and remained stable up to 300°C. The high thermal stability was attributed to the presence of metal-carboxylate clusters in the MOF-5 structure, rather than simple metal ions. This is due to the fact that the metal oxo-cluster forms a stronger bond with the organic ligand than a single metal bonded to a neutral ligand. The synthesis of MOF-5 is illustrated in Figure 1.4.

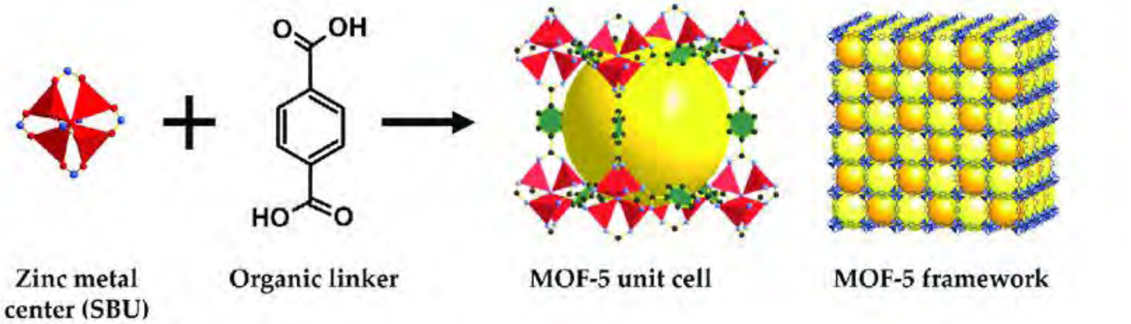

Figure 1.4: Metal-organic framework 5 (MOF-5) is created by combining terephthalic acid and a Zn metal cluster[42].

1.7 Why are MOFs impressive porous materials?

An astonishing 20,000 MOF types have already been documented, and a majority of these have found their way into heterogeneous catalysis, gas storage, gas separation, electrocatalysis, photocatalysis, and biomedicine applications[43].The most alluring characteristic of MOFs lies in their remarkable surface area, reaching an impressive 10,000 m2 /g, equivalent to the vastness of a soccer field. Learned scientists have envisaged a prospective cap of 14,600 m2 /g for MOFs’ surface area, indicating that a mere gram of material would engulf 2.7 American football fields. Hitherto, only two MOFs, namely NU-109 and NU-110, have demonstrated a maximum surface area of 7000 m2 /g. Table 1.1 enumerates the BET surface area and pore volume of some renowned MOFs.

Table 1.1: Surface area of selected MOFs

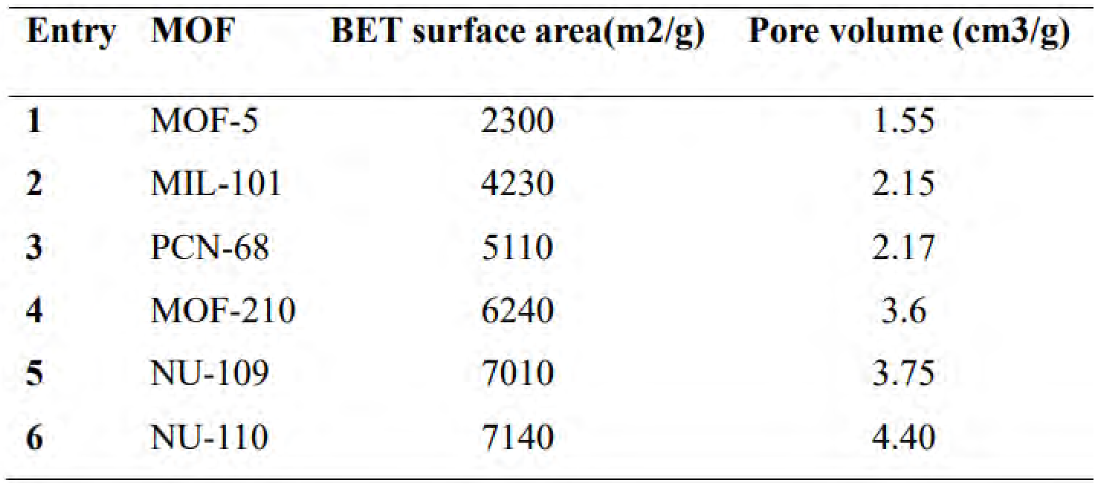

Entry	MOF	BET surface area(m2/g)	Pore volume (cm3/g)
1	MOF-5	2300	1.55
2	MIL-101	4230	2.15
3	PCN-68	5110	2.17
4	MOF-210	6240	3.6
5	NU-109	7010	3.75
6	NU-110	7140	4.40

The second notable characteristic of MOFs pertains to their structural malleability. They possess the ability to conform their arrangement to suit the ingress of extraneous entities, be it liquids or gases, without any disruption to their atomic bonds or alteration to their topological configuration. This phenomenon is referred to as the “breathing effect” and is made possible by the reversible expansion and contraction of the MOF channels/pores. A salient example of this effect is demonstrated by the chromium phthalate (MIL-101), whose cell volume undergoes a significant 30% change during hydration and dehydration[44].

1.8 Applications of MOFs

By means of efficient coordination between metal nodes/clusters and linker molecules, one can fabricate polymeric MOFs. When selecting the appropriate MOF components, it is possible to obtain ultrahigh porous crystals with exceptional thermal and chemical stability. These characteristics render MOFs amenable to chemical modification for a variety of purposes such as CO2 capture, gas storage, drug delivery, catalysis, and a multitude of other applications[45].

1.8.1 MOFs for gas storage and gas separation

Microporous MOFs exhibit immense potential as storage materials for gases, thanks to their remarkably high specific surface area and superior surface-to-volume ratio. A cylinder filled with MOF can store a significantly larger amount of gas than an empty one, owing to the adsorption on the material's surface. The two most prominent MOFs for gas storage, HKUST-1 and MOF-5, are known for their porous structure and extensive BET surface area. In the case of hydrogen, the most effective approach to augment MOF's gas storage capacity is to initiate free metal active sites on the surface for coordination. MOF177, consisting of [Zn4O]6+ metal-oxo-clusters linked by BTC, boasts a remarkable BET surface area of 4630m2/g and is a benchmark material that stores 7.5 wt. % of H2 with a volumetric capacity of 32 g/L at 77 K temperature and 70 bar pressure[21]. The act of separating mixtures stands as a crucial measure in the chemical industry, accounting for approximately 15% of the global energy demand. As such, the separation of gases holds immense significance in the industry, with particular emphasis on the separation of CO2 to mitigate the adverse effects of the greenhouse effect. Chen et al. have ingeniously developed a mix-matrix membrane by combining flexible MIL-53(Al) nanoparticles and polyimide, demonstrating exceptional selectivity (77) as well as a substantial separation factor (53) for the separation of CH4/CO2 mixture.

1.8.2 MOFs as catalysts

Metal-Organic Frameworks, commonly known as MOFs, exhibit a plethora of fundamental properties that render them highly promising materials for heterogeneous catalysis. These materials are endowed with a high density of active sites, accompanied by an extensive surface area and micropores, which serve to bolster their catalytic properties. The presence of single metal atoms, metal clusters, and functionalized linkers in MOFs confers upon them enhanced kinetics, mass transport, and stability, thereby rendering them well-suited for catalytic applications. It is noteworthy that the catalytic properties of MOFs are intrinsically linked to the inorganic metal ions/nodes and ligand functional groups that are present in the pores, channels, or at the outer surface. MOFs have been found to be efficacious in various types of heterogeneous catalytic reactions, including CO oxidation, CO2 reduction, catalytic hydrogen production from water and chemical hydrides, oxidation of alcohols, hydrogenation reaction, catalytic remediation of pollutants, and degradation of organic pollutants[46].

1.8.3 MOFs as drug carriers

MOFs are an exceptional category of nanomaterials that serve as a valuable drug carrier owing to their well-defined structure, adjustable composition and shape, high specific surface area, customizable pore size, and easy chemical functionalization, as expounded in Chapter 1 16. Furthermore, MOFs have shown promising results in the medical field due to their uncomplicated nano-scale synthesis and surface chemistry functionalization. MIL-100/101, MIL-53 (Fe), and MIL-100 (Fe) have been utilized in numerous drug delivery applications with great success[47] With the aid of cutting-edge robotic technology, researchers have innovated MOFBOTs, based on ZIF-8, that proficiently transport and release drugs at a specific location. These miniature machines traverse intricate pathways via artificial flagella under the influence of a magnetic field [48].

1.8.4 MOFs as sensors

Developing highly effective sensing materials that exhibit exceptional performance in the accurate, swift, and delicate identification of organic compounds, gases, and explosives is an absolute necessity for ensuring the well-being of the people and the environment. The gas sensor industry is worth billions of dollars, and semiconductor metal oxides (SMOs) play a significant role in it; however, their intrinsic lack of selectivity has hindered their progress. To enhance their sensitivity, scientists have resorted to designing porous nanostructures with remarkably high surface areas and advanced catalytic functionalities that can optimize the number of gas adsorption sites. In this regard, metal-organic frameworks (MOFs) have emerged as a promising alternative for various sensing applications, especially for gases and small aromatic compounds, thanks to their high surface area, adjustable pore sizes, controllable functional sites, and fascinating physiochemical properties. The hybrid sensors comprising of ZIF-8 (MOF) coated ZnO (SMO) nanowires have exhibited tremendous potential in the detection of hydrogen in the mixture of C6H6 and C7H8. The MOF porous structures have been found to amplify the absorption of species, while the well-defined pores aid in molecular sieving. These characteristics are expected to substantially enhance the sensitivity and selectivity of the sensor. Another noteworthy example is the MFM-300 (In), which can selectively detect the harmful SO2 as compared to CH4, CO2, NO2, and H2, with an impressively low detection limit of 5 ppb [49].

1.9 Zeolitic-Imidazolate Frameworks (ZIFs)

Zeolitic imidazolate frameworks (ZIFs) are a kind of metal-organic framework (MOF)with porous crystal structure that is topologically similar to zeolites[50]. ZIFs are made up of tetrahedrally-coordinated ions made up of transition metals (such as Fe, Co, Cu, and Zn) linked together by imidazolate linkers and these linkers are comparable to the ligands of aluminosilicate zeolite which serves as the organic linker. The fundamental constituent of ZIFs is made up of metal ions, imidazolate, and derivatives. They are bound at a 145° angle, similar to the Si-O-Si angle in zeolites [51] as shown in figure 1.5

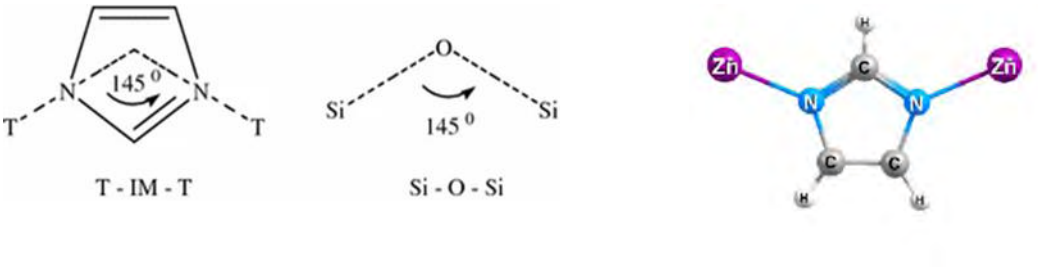

Figure 1.5: The metal-imidazolates in ZIFs and the Si-O bond angle in zeolites are being compared. [52]

The formation of ZIF depends on imidazolate and solvent used. By using modified imidazolate ligands, ZIFs can have more diverse structures [53]. ZIF materials mimic standard zeolites with various topologies using special ligands. ZIFs have the porous structure and stability of zeolites and the adjustability of MOFs. The diversity of ZIFs is impressive [20]. Through advanced synthesis methods, a plethora of new ZIF structures were found. By 2010, over 105 ZIF materials with various compositions and structures were reported. The inherent porosity, abundance of functions, and remarkable stability of ZIF materials offer vast applications. Scientists can modify ZIFs to fit various uses like gas storage, catalysis, drug delivery, sensing, etc. This can be done by using different metal ions and imidazolate ligands [54].

1.10 Role of ZIF-7 mixed with composite Zeolite

Among the several ZIF, ZIF 7 is the one I'm working on. It features a hexagonal SOD structure produced by connecting Benz imidazolate (Bim) anions and zinc cations. The zinc cations serve as metal nodes, with benzimidazole linkers connecting them to form a coordination network.

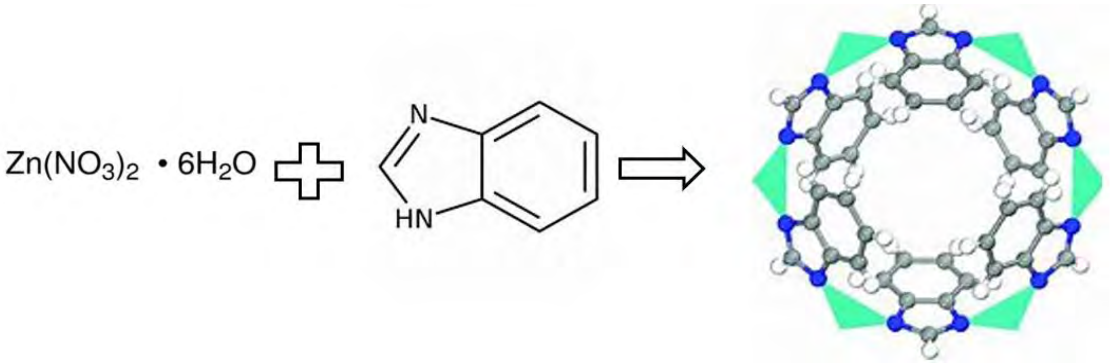

Figure 1.6: Constituent elements of ZIF-7

ZIF-7 has a zeolitic structure, which is comparable to zeolites, and this is where the term "Zeolitic Imidazolate Framework" comes from. The zeolitic structure produces an incredibly porous material with interconnecting channels and cavities. Both ZIF-7 and Zeolite have SOD topology and porous structure. The Benz-imidazolate linkers in the ZIF-7 structure play an essential role in determining the size and geometry of the pores. The particular coordination between organic linkers and metal cations impacts the material's overall stability and porosity. Due to its porous ang highly flexible structure, it allows the guest molecules in its structure[55].

Zeolites are crystalline aluminosilicate minerals that can be natural or manufactured. They are made up of a three-dimensional framework of SiO_4 and AlO_4 tetrahedra linked together by oxygen atoms. Zeolites feature a systematic array of uniformly sized channels and cages known as micropores. These micropores are essential for the adsorption and ion-exchange characteristics of the material.

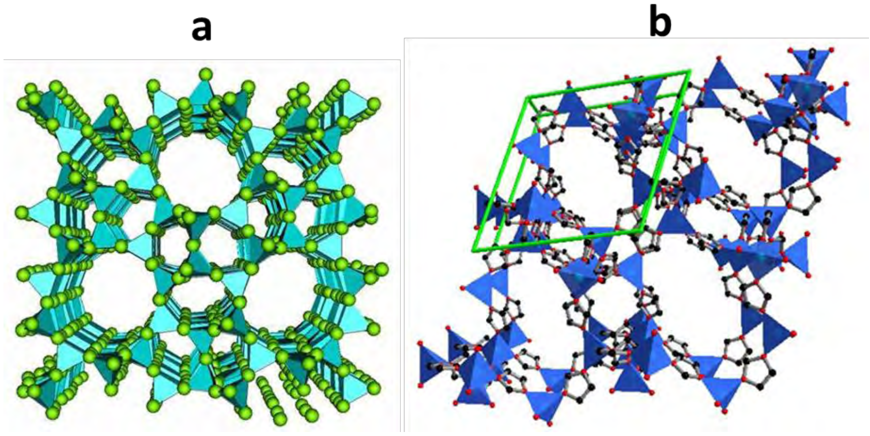

Figure 1.7: Comparison in the structures of (a) Zeolite (b) ZIF-7

Depending upon certain conditions there is phase shift in ZIF -7 structure. The first phase is designated as ZIF-7-I more often called ZIF-7 and it has rhombohedral unit cell ($R\bar{3}$space group). The second phase is known as ZIF-7-II with a triclinic unit cell ($P\bar{1}$space group). Both these phases are reversible into each other. The third phase is known as ZIF-7-III has a monoclinic unit cell (C2/c space group). ZIF-7-III has a two-dimensional (2D) layered architecture that is made up of four-membered rings of corner-shared networks of Zn (II) benzimidazole[56]

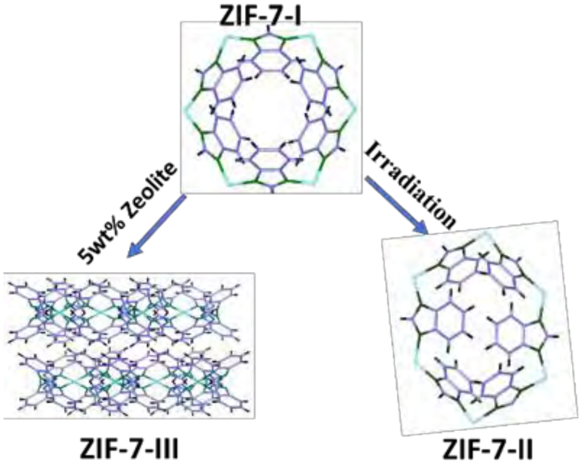

Figure 1.8: Phase Transitions of ZIF-7 Phase

From the literature I have found that there are several ways to synthesize ZIF-7-I and certain conditions upon which there is phase transformation in ZIF-7-I structure[57].

Table 1.2: Phase transformation in ZIF-7 structure

ARTICLES	ZIF-7-I	ZIF-7-II	Conclusion
[57]	With DMF Rhombohedral structure Doublet peaks	Without DMF Triclinic structure Multiple peaks	• On heating ZIF-7-I was converted to ZIF-7-II. • Removing guest molecules from ZIF-7-I it turns into ZIF -7-II. • ZIF-7-II is converted to ZIF-7-III by leaving ZIF-7-II in water for a week.
[20]	Without CO_2 T<308K	With CO_2 T>308K	• ZIF-7-II is converted to ZIF-7-I on giving CO_2 pressure and vice versa.
[56]	With DMF rhombohedral unit cell ($R\bar{3}$space group)	With out DMF triclinic unit cell ($P\bar{1}$space group)	• ZIF-7-I is converted to ZIF -7-II on applying different heating conditions. • ZIF-7-II is converted to ZIF-7-III upon liquid intrusion.
[41]	With guest molecules like DMF	Without guest molecules	• ZIF-7-I was converted to ZIF-7-II at 154 C in the Prescence of N_2. • At 25C with CO_2, ZIF-7-II was transformed into ZIF-7-I.
[58]	With guest molecules like DMF	Without guest molecules	• ZIF-7-I was converted to ZIF-7-II when guest molecules were removed from ZIF-7-I.

ZIF-7's structure provides it with a large surface area and a pore size of 0.3nm. Pores are microporous, which means they have diameters in the nanoscale range, making them excellent for gas adsorption as well as storage applications. ZIF-7 has been investigated for a variety of applications due to its peculiar structure and features, such as gas separation, storage of gases such as hydrogen and carbon dioxide, and catalysis[59]. Its promise for gas storage as well as separation stems from the microporous framework's capacity to selectively adsorb and store certain gases. Some ZIFs, such as ZIF-7, have structural flexibility, which allows them to go through reversible structural changes in reaction to external stimuli such as changes in temperature and pressure or incorporation of guest molecules. By tolerating guest molecules inside the framework, they can improve the gas's adsorption capacity along with selectivity. Due to its small pore size, it is widely used for carbon capture as the pore size of carbon dioxide is 0.32nm [60].

To enhance the properties of ZIF-7, I added the zeolite as a composite and zeolite also have remarkable properties and when they both combine together to make a composite material, a hybrid material with synergistically favorable qualities is formed. When these two unique kinds of porous materials are combined, their distinctive properties may be integrated, resulting in new capabilities and possible applications and also there is phase transformation in ZIF-7 structure. Here are some of the potential results and benefits of mixing zeolites with ZIFs [61]:

Zeolites have well-defined microporous structures, whereas ZIFs have an adjustable porous network. By mixing the two distinct materials, the composite may have a larger range of porosity and shapes, resulting in higher porosity and surface area. This increased porosity may lead to increased gas adsorption capacity and selectivity. Zeolites are noted for their high thermal as well as chemical stability, but ZIFs might be sensitive to environmental factors. Mixing zeolites alongside ZIFs may improve the composite's overall stability, making it more resistant under a variety of operating situations. Because of their distinct active sites, zeolites and ZIFs may both operate as catalysts for various processes. When these materials are combined, they can form a composite with unique catalytic activity, possibly enhancing the reaction's effectiveness and selectivity. The capacity of ZIFs to trap guest molecules inside their porous structure is well established. When integrated with zeolites, the composite material may have unique guest molecule encapsulation capabilities, which might lead to applications in controlled medication administration and molecular sensing[62].

The zeolite-ZIF composite's specific characteristics and functions are determined by factors such as the zeolite plus ZIF components employed, the corresponding structures, and the manufacturing technique used to generate the composite.

1.11 Electrochemical Water Splitting Mechanism

The water electrolysis process consists of two half-reactions: oxygen evolution and hydrogen evolution. The pH at which the electrolysis process takes place affects these half-equations slightly. At low pH, the HER and OER proceed as follows.

$$\mathbf{4H^{+} + 4e^{-} \longrightarrow 2H_2 \ldots\ldots\ldots\ldots\ldots\ldots (1.8)}$$

$$\mathbf{2H_2O \longrightarrow O_2 + 4H^{+} + 4e^{-} \ldots\ldots\ldots\ldots\ldots\ldots (1.9)}$$

To electrolyze water, a lot of electrical energy is needed. The minimum voltage required for this is 1.23 V. However, additional voltage is required to overcome various barriers, which is called overpotential. This includes concentration, ohmic resistance, and kinetic overpotential [13]. A relevant benchmark for solar-powered electrolyzers is 10 mA cm^{-2}. OER's excessive potential is a challenge due to the four-electron, four-proton process for O2 formation [63].

A chemical reaction's mechanism is a possible or projected path that is pursued during the whole process under certain conditions. The potential of the cells and mechanism that regulate the complex and multi-step electrochemical splitting of water reaction is identified through the half-cell reaction, such as OER or HER, and are strongly dependent on the pH of the reaction medium (as indicated in Figure 1.9). In basic terms, the presence of different ions (such as H+ or OH-) inside the reaction medium has the ability to change the energy level and chemistry of the electrolyte, hence altering the pathways of reaction that underpin the entire chain conversion process of water splitting.

1.11.1 Oxygen Evolution Reaction (OER)

The Oxygen evolution reaction (OER) is the inverse of the ORR and is commonly used to couple with other processes in a variety of critical sustainable power frameworks, including solar cells, metal-air batteries, and electrochemical splitting. The Oxygen evolution reaction (OER) is a restrictive reaction that happens throughout the chemical processes that produce molecular oxygen. For example, O2 is produced during photosynthesis as the outcome of water oxidation, while water electrolysis creates O2 and H2. Furthermore, O2 is formed from oxides and oxoacids. Better OER catalysts are critical for the growth of numerous sustainable power technologies, including solar power production and metal-air batteries[64].

Despite the fact that precious metal oxides, like ruthenium and iridium oxides, have the highest OER performance, their rarity and high cost have limited their diverse uses. The key difficulty at the moment is to investigate alternate non-precious metal catalysts for the production of the kinetically slow OER. The process that governs of OER amid acidic and alkaline conditions is depicted in the figure1.9.

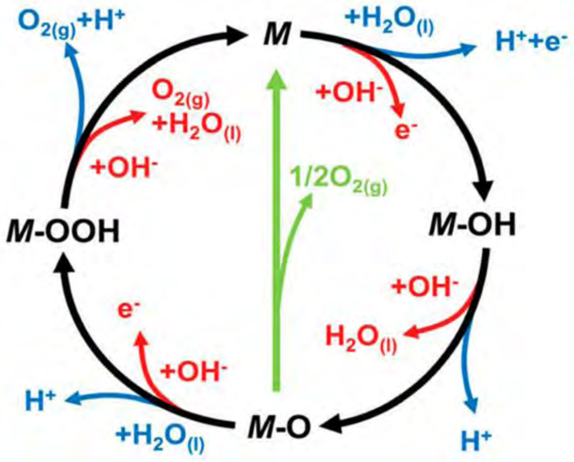

Figure 1.9: OER mechanism in acidic and alkaline medium[65]

1.11.2 Aeration Evaluation Mechanism

The formation of O2, electrons, and protons occurs as a result of the OER method, one of the two half-cell reactions. Each step has a positive Gibb's free energy and is thermodynamically uphill. Numerous methods for OER for duo acidic and basic environments have been proposed. The process depicted in the figure is the most well-known and thoroughly studied one, and it involves the formation of numerous intermediates (M-OH*, M-O*, and M-OOH*) [66].

$$\mathbf{OH^- + M \longrightarrow M\text{-}OH + e^- \ldots\ldots\ldots\ldots\ldots (1.10)}$$

$$\mathbf{M\text{-}OH + OH^- \longrightarrow M\text{-}O + e^- + H_2O \ldots\ldots\ldots\ldots (1.11)}$$

$$\mathbf{M\text{-}O + OH^- \longrightarrow M\text{-}O\text{-}O\text{-}H + e^- \ldots\ldots\ldots\ldots\ldots (1.12)}$$

$$\mathbf{M\text{-}O\text{-}O\text{-}H + OH^- \longrightarrow M + O_2 + H_2O + e^- \ldots\ldots\ldots\ldots\ldots (1.13)}$$

Figure 1.12's blue and red lines, representing an acidic and basic medium, respectively, depict the progressive formation and combination of intermediates required for electron and proton transport. The diagram also shows that the blue and black lines represent the direct (M-O combination) and indirect (M-OOH production) routes to completing the water oxidation process cycle, respectively [67].

As seen in the picture, all of these fundamental stages are tightly related to the pH level of the reaction media. Every step in an acidic medium demands the conveyance of electrons and protons, ultimately which leads to the oxidation of a couple of molecules of water during the whole process. Following that, the release of O2 molecules occurs via a process involving the connection of four electrons and protons. The OH-ion takes front stage in the basic medium with a four-electron exchange that results in the formation of O2 and molecules of water. Regardless of the mechanical methodologies used, forecasting the rate determination step stays difficult, while the Tafel slope value acting as a guidepost[68]. Because of the great complexity of OER, the creation of M-OOH (the third phase) is regarded as the most energy-intensive and slower stage, with a high Gibb's free energy. be a result, a reduced Tafel slope (60 mV/dec) is usually referred to be a rate-determining step throughout following phases. The number of electrons/protons exchanged throughout the reaction may also be used to describe the OER process. A Tafel slope value of 60 mV/des indicates a one-electron and one-proton process, while a value of 40 mV/dec implies a two-electron and one-proton linked activity. A two-proton, one-electron process is one in which the Tafel slope is greater than 100 mV/dec [69].

1.12 Benchmarking factors for water electrolysis

The electrolytic dissociation of water molecules may be carried out successfully within a suitable cell with a typical electrode setup consisting of a reference electrode, a counter electrode, as well as a working electrode. A potential controller and a conductive electrolyte must both be used during this procedure. For the redox process in a three-electrode system, the voltage across the working electrode is changed. The specific reaction's thermodynamic laws govern how large the potential range can be. Two electrodes, the anode and cathode, are employed for redox reaction during the separation of water molecules process. In a half-cell reaction, just the working electrode contains catalytic materials and is evaluated using tests. Overpotential, Electrochemical Impedance Tafel slope, and chronoamperometry characteristics are clearly explained.

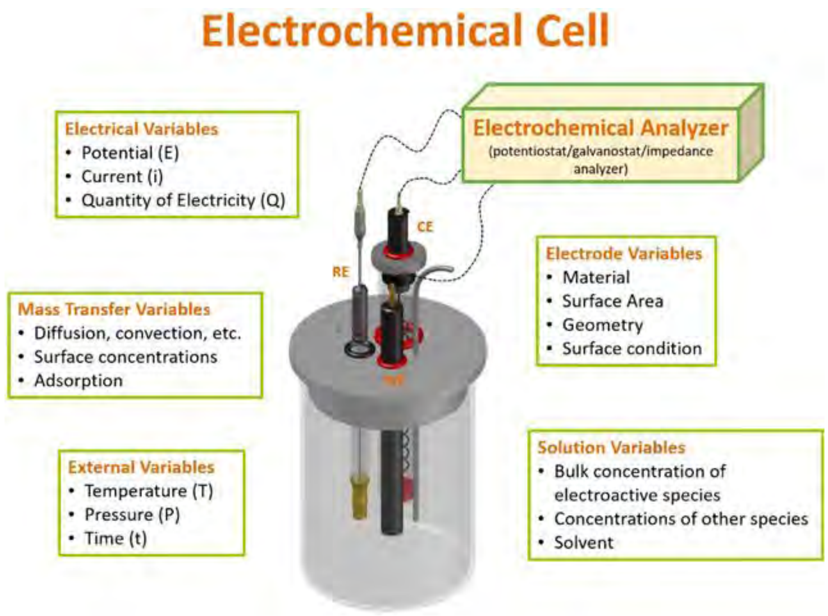

Figure 1.10: Three-electrode electrochemical set-up

1.12.1 Linear Sweep Voltammetry

Linear sweep voltammetry, a well-known electrochemical method, is frequently used to investigate the properties of redox-active components in a solution. This entails exposing an electrode to a linearly increasing voltage while simultaneously measuring the current generated. The collected current-potential data may be represented as a beautiful voltammogram, with the longitudinal axis representing current and the horizontal axis representing potential. This engrossing narrative provides great insights into the intricate redox reactions occurring within the solution[70].

LSV presents a plethora of significant electrochemical characteristics, encompassing:

- Peak Potential (Ep): The point at which the highest current is witnessed.
- Peak Current (Ip): The ultimate current perceived during the voltametric scan.

- Peaks of Anodic and Cathodic nature: LSV can expose the anodic and cathodic currents that correspond to the oxidation and reduction procedures, respectively.
- Half-Wave Potential (E1/2): The point at which fifty percent of the peak current.

  The major factor that we calculated from LSV is over potential.

1.12.2 Overpotential (η)

Overpotential is a crucial quantity that determines the efficacy and natural competence of an electrocatalyst during catalytic processes. In electrochemistry, each reaction has a unique equilibrium potential (EP), and overpotential is the amount of overpotential required to initiate an electrochemical reaction from its EP. The smallest potential required for splitting a single mole of water under typical conditions is the EP for splitting water, which is 1.23 V versus RHE. In an ideal environment, the applied voltage would equal the EP and initiate an electrochemical reaction. Unfortunately, kinetic barriers and ohmic losses break the perfect surroundings around the electrodes in actual applications. As a result, a greater input potential is required, which is referred to as overpotential. Activation overpotential, concentration overpotential, plus resistance overpotential are all examples of overpotential. Utilizing active catalytic materials can enhance the catalyst's natural qualities. Meanwhile, because to restricted diffusion and unequal ion distribution, electrolysis causes a concentration reduction near the electrode. Fortunately, the reaction media may be agitated to regulate this to some extent[71]. The resistance at the system’s interfaces, referred to as the junction resistance, contributes to the overpotential. Inadequate detachment and the development of bubbles upon electrode surfaces can also contribute to overpotential. An electrolysis reaction can start close to the equilibrium potential if there is a low overpotential, which means the conditions for the electrocatalyst and reaction are suitable. To measure electrode effectiveness, current density after initial potential is key. Comparing electrocatalysts needs same pH and temp. Overpotential needed for 10mAcm-2 current density [72].

1.12.3 Tafel Slope

The term “Tafel slope” is commonly used in electrochemistry to describe the relationship between current density (j) and electrode potential (E) during an electrochemical reaction. The voltage and current are the two main factors that determine any electrochemical process, and this is represented by the symbol "" (beta) and is typically measured in terms of volts per decade or millivolts per decade. Adjusting the potential window, is similar to fine-tuning the driving force within an electrode-electrolyte system. Tafel slope analysis is widely accepted as the preferred method for digging inside the kinetics and mechanistic complexities of electrochemical processes. When it comes to complex reactions like OER/HER, the following equation helps clarify the relationship between applied current and potential

$$\boldsymbol{\beta = (d\,(\log j)/dE).}$$

The parameter reflects the Tafel slope in the given equation, whereas d (log j) represents the differential variation in the logarithmic change of the current density (j), and dE represents the equivalent differential variation in the electrode’s potential (E).

Examining the polarization curve in equilibrium will reveal the current density (j), which can then be calculated and plotted against the overpotential. The Tafel slope value, which serves as a comprehensive indication of an electrode process, can be obtained by matching the linear expression of log j versus. This number gives crucial details about the mechanism of the reaction, the step that determines reaction rate, and the kinematics of the entire electrochemical process. In general, lower Tafel slope values suggest a faster electrode process, whereas higher ones indicate the reverse. It is critical to compute this value in the initial potential zone, as the Tafel slope might vary dramatically when selecting either higher or lower potential regions, irrespective for the identical rate-determining step[72]

1.12.4 Chronoamperometry

The critical evaluation of the electrocatalyst’s tenacity is a critical component, especially when considering the possibilities of commercializing this sophisticated technology. The catalyst must be stable at both high and low current densities in order to achieve the smallest onset/over potential. It takes several steps to split water, and many intermediates are produced along the way. This technique is frequently carried out in industrial settings under extreme acidic/basic conditions and at elevated temperatures. As a result, the potential-induced transformation and the hard operating circumstances can drastically reduce the electrocatalyst's long-term lasting and maintained performance. Metal catalysts are recognized for their proclivity to oxidise and achieve a very elevated oxidation state, resulting in the formation of metal oxides having polarity index values that are comparable to water. Unfortunately, this causes the catalyst to move away from the surface of the working electrode and toward the electrolyte. Stability tests can be used to identify inactive phases that may develop on the catalyst's surface. As a result, it's vital to test the long-term performance of electrode materials under commercial electrolyzer-like circumstances for at least 24 hours. It is a critical step in ensuring that the efficacy of the materials used for electrodes is not compromised. Chronoamperometry is generally recognized as an experiment that may be used to assess the stability of catalysts under operating settings. It entails keeping track of the constancy or shift of the current over time for a certain applied potential[73].

1.13 Electrode Potential and Electrocatalysis

The application of a required potential in the discipline of electrocatalysis is accomplished by immersing electrodes into a suitable electrolyte. The probable goal of the origin is to control electrical density for oxidation/reduction process. These electrodes, also referred to as current collectors, are covered in catalytic material, which catalyzes the reaction at the electrolyte-catalyst-electrode contact. During operation, the catalyst is ionically bonded to the electrolyte and electrically connected to the electrode. Electrodes spark reactions with help from catalysts. Catalysts quicken transfer and stabilize intermediates. The modulation of reaction pathways occurring on electrode surfaces can result in a reduction in the activation energy of different intermediates in the field of electrochemistry. The practicality of a water division procedure under specified conditions is determined by its initial potential at the given potential. The redox reaction flow in electrocatalysis, like that of other catalytic processes, is dependent on the comparable orbital energy levels at the electrode-electrolyte interface. The sensitivity of electrochemistry is highlighted by electrons' ability to switch between orbitals with higher and lower energies. The difference in potential between the electrodes and even the potential/electronic density at the electrode-electrolyte interface can be carefully controlled in a half-cell reaction. The lowest unoccupied molecular orbital (LUMO) and highest occupied molecular orbital (HOMO) energies decrease as a result of the anodic polarization, which removes electrons from the electrode-deposited catalyst. As a result, electrons move from the electrolyte in one direction towards the catalyst, which acts as a sink. In order to complete the cycle by converting electrons to protons, which act as the sink in the water splitting reaction, electrons move from the electrolyte, specifically H_2O, to the cathode, which serves as the source. The mechanism of redox reactions at the outer layer of the electrodes may be made feasible by the presence of the necessary cell potential. The type and inherent capabilities of the electrocatalyst, however, play a significant role in enabling the transport of charged species while adhering to the Sabatier principles, allowing these reactions to proceed effectively and rapidly with minimal potential. In order to achieve a continuous adsorption/desorption process for catalytically assisted processes, the Sabatier principle emphasizes the significance of a strong bond between the catalyst and the intermediates [72]. Unwanted desorption of intermediates reduces the likelihood that new incoming intermediates will be able to access active sites if the catalyst-intermediate contact is overly strong. On the other hand, a weak interaction interferes with the catalyst's active sites and does not support the proper stabilization of intermediates. It also hinders perfect electron exchange. The inherent catalytic capabilities of electrocatalysts can therefore be tuned to ensure the best interaction and activation of various intermediates through structural and electrical engineering of electrode materials [69].

1.14 Research Objective

The goal of this research is to synthesize the different polymorphs such as ZIF-7 and its composite with Zeolite using solvothermal technique and in-situ method. The goal of this research is to create an efficient electrocatalyst to promote water-splitting specifically focused on the production of O_2. The efficacy of the electrocatalyst in OER is going to be tested using extensive electrochemical tests such as LSV, EIS, Tafel Slope and Chronoamperometry for its long-term durability and stability. The porous structure of both ZIF-7 and Zeolite will produce an efficient electrocatalyst which will enhance the electrocatalytic activity. By changing the concentration of Zeolite in ZIF -7 we will see the effect of our electrocatalyst on water splitting and catalytic activity. The ultimate objective is to contribute to the progress of water splitting technologies for environmentally friendly hydrogen and oxygen generation, renewable energy storage, metal air batteries, fuel cells, and other relevant applications, therefore encouraging a greener and more energy-efficient future.

CHAPTER 2

2. EXPERIMENTAL

This chapter elucidates the distinct synthesis methods employed for the production of ZIFs material. Moreover, it itemizes the chemicals implemented in the synthesis of ZIF-7, and their composites. The main emphasis is placed on the discourse of the synthesis protocols, techniques, and an overview of the characterization methods employed.

2.1 Synthesis Methodology

This section elucidates the Protocols for synthetic reactions, encompassing the type, purification, and analysis of porous coordination polyhedral. Nanomaterials have a myriad of applications, and their performance is significantly impacted by their size and shape. Therefore, there is a concerted endeavor to regulate the synthesis of nanomaterials. The controlled preparation of ZIF-7 and its composites is of paramount importance given the vast gamut of applications these nanomaterials possess. Due to its high surface area and tunable pore size, it is used in gas separation and storage, catalysis, drug delivery, sensing and detection, water remediation and energy storage and conversion. The challenge of these nanoparticles potentially growing into large, asymmetrical particles is one that must be addressed. Furthermore, the phase purity of the final product presents the scientists with an additional obstacle to overcome. To mitigate these challenges, it is necessary to promote a more reliable and straightforward preparation technique to obtain pure nanomaterials. The current work utilized simple mixing techniques, including stirring and sonication. This method is expeditious, uncomplicated, and does not require the use of expensive toxic materials or a catalyst. Consequently, it is the optimal approach for producing nanomaterials at a low cost.

2.2 Chemicals and reagents:

Utilization of superior synthetic compounds and solvents in the synthesis of materials has ensured the attainment of purity in the final product. Sigma Aldrich (Germany) facilitated the procurement of zinc nitrate, benzimidazole, KOH pellets and zeolite which were utilized without further purification as a solute. The solvents which were used are N, N

Dimethylfouride, Ammonia solution and Methanol all these solvents were purchased from Sigma Aldrich Company. The deionizer system of the laboratory was the source of the deionized water utilized in the preparation of the electrolyte. For the creation of the electrolyte, KOH pellets are also imported from the prestigious Sigma Aldrich in Germany.

2.3 Solvents for drying:

Ethanol, methanol, and deionized water were utilized in the synthesis process. The solvents were dried before use to eliminate moisture and impurities.

2.4 Dehydration of ethanol and methanol:

To obtain pure ethanol and methanol, the usual drying process was used with magnesium turnings, and iodine crystals were used as a marker.

2.5 Different Synthesis techniques of ZIFs materials:

There exists a plethora of techniques available for the creation of ZIF, each with its own unique approach and flair.

- Solvothermal/Hydrothermal
- Microwave-aided synthesis
- Sono chemical technique:
- Synthesis through electrochemistry:
  Mechanochemical Synthesis of ZIF

2.5.1 Solvothermal/Hydrothermal

Hydrothermal synthesis is a unique process that creates single crystals by precipitating substances from high-temperature aqueous solutions. This method is also known as the hydrothermal method. It relies on the minerals’ solubility in hot water under immense pressure. A magnificent steel pressure vessel, the autoclave, fosters crystal growth. Nutrient and water combine, and a temperature gradient is created. The nutrient solute dissolves at one end, while at the other end, it is deposited on a seed crystal, leading to the desired crystal's growth [74].

The hydrothermal method of crystal growth is superior to others as it can produce unstable crystalline phases. It can also cultivate materials with high vapor pressure and generate large, high-quality crystals with controlled composition. However, this approach does require expensive autoclaves, and observing crystal growth is impossible if employing a steel tube[1Oref]. Nonetheless, autoclaves made out of thick-walled glass may be utilized up to temperatures of 300°C and 10 bar[75].

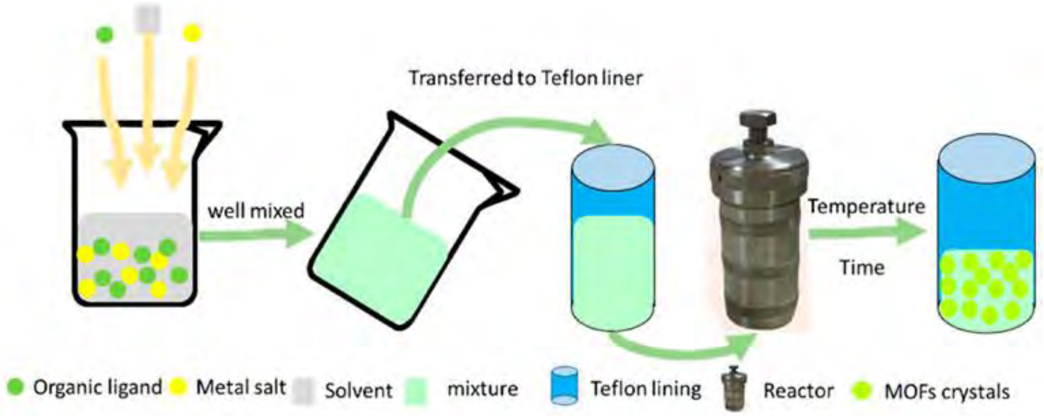

Figure 2.1: Demonstration of the hydrothermal procedure through the utilization of an autoclave[76].

2.5.2 Microwave-aided synthesis

Microwave-assisted synthesis techniques frequently used for rapid nano porous material synthesis in hydrothermal conditions. This method offers phase selectivity, particle size control, and uniform energy absorption for easy morphology control. Microwave synthesis equipment has power output control and fiber optic temperature and pressure sensors [77].

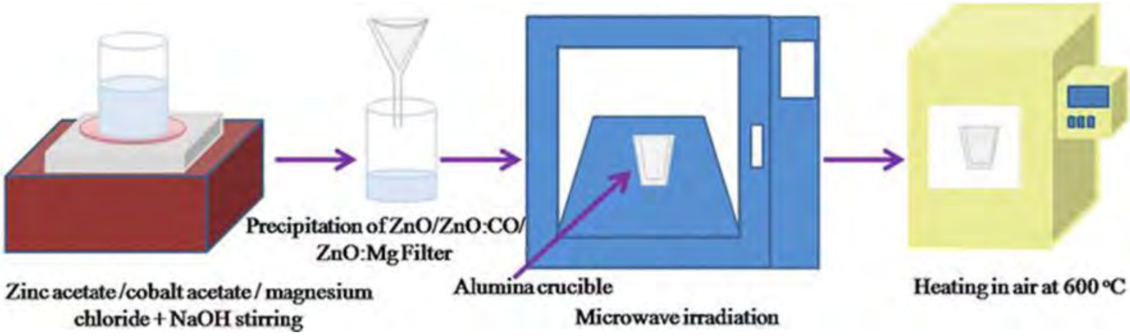

Figure 2.2: a schematic diagram depicting the process of heating [78].

2.5.3 Sono chemical technique:

The magic of Sono chemical synthesis includes using high-energy ultrasound to quicken the reaction mixture, leading to smaller and more uniform particle size than traditional solvothermal synthesis. In Sono chemical synthesis, bubbles called acoustic cavitation form and collapse, resulting in high local temperatures and pressures. This leads to rapid heating and cooling rates, improving the process kinetics [46].

2.5.4 Synthesis through electrochemistry

Electrochemical synthesis possesses various advantages, namely:

(1) Synthesize swiftly and coolly, unlike traditional methods.
(2) The absence of metal salts makes it unnecessary to separate anions like NO3- or Cl- from the synthesis solution.
(3) the linker's full use may become a reality [79].

The key synthesis principle involves providing metal ions to a mixture of organic linker and electrolyte. However, the process also produces H2 from dissolved organic linker molecules.

2.4.5 Mechanochemical Synthesis of ZIFs

Mechanochemical synthesis is the art of breaking internal bonds mechanically, then transforming them chemically [73-75]. The synthesis can occur without solvents at room temperature, thus avoiding the use of organic solvents [54]. The method quickly produces high yields, typically within 10-60 minutes. The resulting products are usually made of tiny particles. Metal oxides are commonly used as substrates with water being the only byproduct [80]. Adding a tiny amount of solvent, called liquid-assisted grinding, boosts mechanochemical reactions by making the reacting molecules more mobile. This liquid can also help shape the resulting structures. Beldon et al. reported making ZIFs with mechanochemical methods. They converted ZnO into HIM, HMeIM, and HEtIM-based ZIFs, porous and nonporous, in 30-60 minutes [81]. LAG was found to speed up and regulate phase formation, while ammonium ions aided ZIF synthesis [43, 54]. Moreover, the group conducted a live investigation on mechanochemical changes in a ball mill using high-energy synchrotron X-ray analysis [82].

Figure 2.3: Schematic diagrams have been presented to illustrate the process of solvent-free synthesis of MOFs from solid materials[83]

2.6 Synthesis of ZIF-7-I:

The ZIF-7 was successfully synthesized by conventional hydrothermal method, following the procedures given elsewhere [24]. All chemicals, zinc nitrate hexahydrate (Zn (NO3)2.6H2O), benzimidazole (C7H6N2, 98%, Aldrich), N, N-dimethylformamide (DMF) (99%, Aldrich), and methanol (CH3OH, 99%, Aldrich), were used as- received without further purification. A solid mixture of zinc nitrate hexahydrate Zn (NO3)2.6H2O (0.8025 g, 2.7 mmol) was dissolved in 36 ml of N, N-dimethylformamide (DMF) through sonication for half an hour. Concurrently, benzimidazole (0.2347 g, 2 mmol) was dissolved in 36 ml of methanol through sonication for the same duration. Following this, the solutions were mixed together through sonication for an additional half hour. After half an hour when the solution turned lime 10 ml of ammonia solution was added to the newly made solution and stirred for 20 minutes, resulting in a white solution. The homogeneous solution was then transferred to a Teflon lined stainless steel autoclave and tightly capped. The autoclave was positioned in an oven for six hours at 130C. Once done, the autoclave was cautiously removed from the oven and allowed to cool at room temperature. The solution was then meticulously extracted from the autoclave and placed into a beaker. The solution was then centrifuged and washed with methanol thrice. The semisolid solution was then poured into a Patri dish and dried at 80C. Eventually, white crystals of ZIF-7-I were collected in a glass veil.

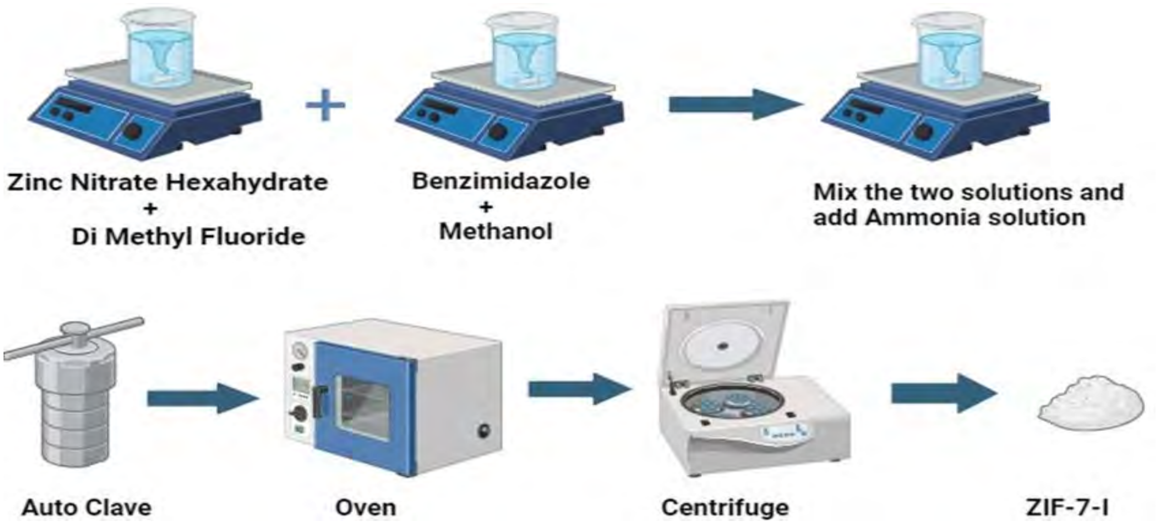

Figure 2.4: Synthesis of ZIF-7-I

The ZIF-7-I nano porous host structure allows for easy loading and unloading of guest molecules due to its flexible framework[59].

2.6 Synthesis of ZIF-7-I/Zeolite

A solid mixture of zinc nitrate hexahydrate Zn $(NO3)2.6H2O$ (0.8025 g, 2.7 mmol) was dissolved in 36 ml of N, N-dimethylformamide (DMF) through sonication for half an hour(S1). Concurrently, benzimidazole (0.2347 g, 2 mmol) was dissolved in 36 ml of methanol through sonication for the same duration(S2). Following this add 1.25wt% and 5wt% of zeolite in already prepared benzimidazole methanol solution(S2) by in-situ method respectively and sonicate it for 30 minutes. Following this, the solutions S1 and S2 were mixed together through sonication for an additional half hour. Subsequently, 10 ml of ammonia solution was added to the newly made solution and stirred for 20 minutes, resulting in a white solution. The homogeneous solution was then transferred to a Teflon lined stainless steel autoclave and tightly capped. The autoclave was positioned in an oven for six hours at 130° C. Once done, the autoclave was cautiously removed from the oven and allowed to cool at room temperature. The solution was then meticulously extracted from the autoclave and placed into a beaker. The solution was then centrifuged and washed with methanol thrice. The white semisolid solution was then poured into a Patri dish and dried at 80° C. By adding 1.25w% of zeolite in ZIF-7-I is turned into mixture of Z-7 (I+III) by adding 2.5wt% of zeolite in ZIF-7-I it was turned into Z-7-III and by adding 5w% of zeolite ZIF -7-I it was turned into Z-7-III. On increasing the concentration of Zeolite onwards from 2.5wt% there was no change found in the structure.

2.7 X-Rays Diffraction (XRD):

The X-ray diffraction method is used to assess if a material is crystallized or amorphous. It is used to determine the unit cell of the sample as well as the phase of the specimen's structure. The XRD method makes advantage of the X-ray dispersion phenomenon induced by a lattice of atoms. X-rays are a kind of electromagnetic radiation with a high intensity and a short wavelength, generally between the 0.01 and 10 nm [42]. Diffraction demands that the spacing between the atoms be equal to or greater than the wavelength of the X-rays. Cu and Mo (1.54 and 0.8, respectively) are commonly employed to create X-rays with structures comparable to those in our sample. The regularly ordered crystal structure acts as though genuine 3-D diffraction is occurring.

Energy of X-ray photons is given by

$E= h\vartheta$ OR $E= hc/\lambda$................ (2.1)

if λ= 0.0998nm and hc= 1240 eV. Nm

then E= 12.42 Kev.............................. (2.2)

In order to study the crystalline structure of materials, the material's energy region should be within 10 keV and 5 keV. X-ray photons with this energy (10 keV to 50 keV) can get beneath a crystal layer and either be absorbed or dispersed by these atoms; this scattering and absorption is the cornerstone of the unidentified structure investigation.

Below are a few benefits of X-ray diffraction[84]

X-ray diffraction is a rapid, effective, and widely used technology.

- It is also a low-cost procedure. Because air is unable to absorb X-rays, there is no need to place the specimen in a vacuum.
- The XRD machine requires measurement instruments, which are easily accessible.
- XRD simplifies data interpretation tremendously.
- XRD requires only a little amount of sample.

W.H. and W.L. Bragg suggested X-ray diffraction for the first time. In 1913, scientists found that a crystalline substance would bounce back X-rays with the exact same phase as the incoming wave. Bragg's law demonstrates the periodic atomic structure of the crystal. Because X-rays have a very short wavelength and a very high energy, studying X-ray diffraction by crystal is comparatively straightforward. A crystal operates as a 3D diffraction grating because atoms are organized in predictable planes with spacing equivalent to the wavelength of x-rays. Using an X-ray beam, we may now explore the structure of every state of matter. The sole criterion is that the incident wavelength matches the interatomic distance of the given sample. If both identical-wavelength x-ray beams (a and b) collide, they will return from two consecutive planes. The interplanar distance is defined as the distance d among these planes. The incident beam makes a -shaped angle with the crystal's plane.

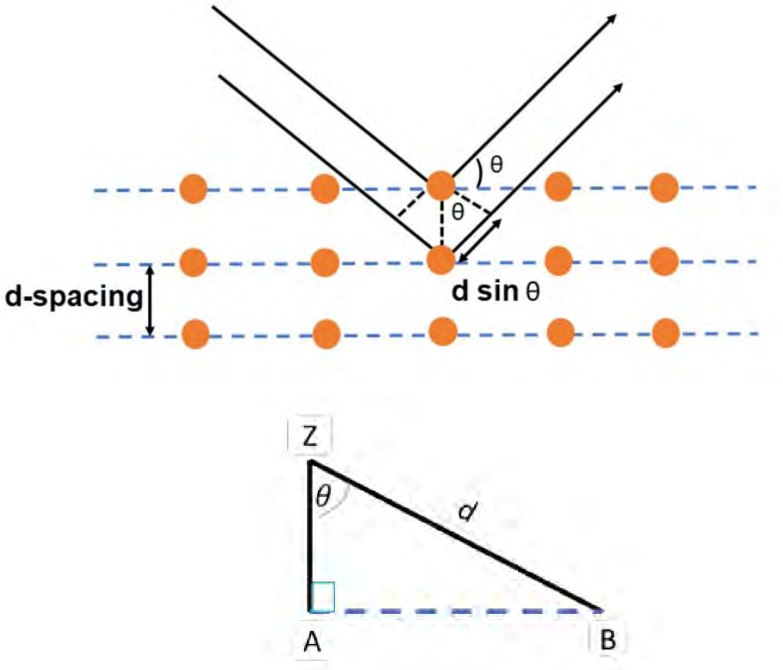

Figure 2.5: X-rays reflecting off adjacent planes[85]

We have drawn two perpendiculars from Z to A and C to calculate the d, i.e., path difference, between these X-ray beams a and b.

$$\text{Path difference} = AB + BC$$

$$AB = d \sin\theta \quad , \quad BC = d \sin\theta$$

Path difference = d sinθ + d sinθ , Path difference = 2d sinθ

When these reflecting beams interact constructively, we will see a brilliant spot on the screen (photographic plate). Because the path difference between these beams is an integer multiple of the wavelength, they will remain in phase. Bragg's diffraction occurs when the positive interference path difference equals n. This is known as Bragg's law. Here, n represents positive integers (n = 1, 2, 3, etc.) and is the wavelength of the incoming X-rays. If we know the wavelength of the X-rays when they strike the sample, we can readily calculate 'd' (interplanar spacing). Crystal structure study relies upon the X-ray diffraction technique.

To examine the sample's structure for crystalline or amorphous formations. The method is known as X-ray diffraction. The X-ray diffraction graph shows their structure. If the sample is crystallized, the pattern will be exceedingly sharp and will have several peaks. It proves that the material is made up of periodic elements. If the material has an amorphous structure, the graph will have one or two sharp peaks.

The full width, half maximum rule (FMHW) can be used to assess if a material is polycrystalline. In mathematics, the equation is,

$$\mathbf{S} = \frac{0.9\lambda}{B\,Cos\,\theta_B} \quad \ldots\ldots\ldots\ldots\ldots\ldots\ldots\ldots\ (2.3)$$

S denotes the grain size, R the wavelength, o the Bragg's angle, and A the full width half maximum. and the whole width at half maximum is illustrated below.

$$\mathbf{A = 1/2*[2\theta_1 - 2\theta_2]} \quad \ldots\ldots\ldots\ldots\ldots\ldots\ (2.4)$$

To calculate the unit cell's density, we employ the formula

= sum of atomic weight of all atoms

NA = Avogadro's number

V = Volume of the unit cell

figure 2.10 depicts powder X-ray diffraction data. The sample is placed on a flat plate, which is then rotated along an axis parallel to the rotating disc. There is a slit that allows the monochromatic radiation produced by the X-ray tube to flow through. The diffraction phenomenon occurs when the sample is subjected to an X-ray beam. The amplitude of the diffracted rays is measured by a counter. The X-ray source, sample, and counter are all located in the same plane. The counter has axis rotating capabilities. The specimens that we produced before are being characterized using XRD analysis. The Burker XRD machine and D8 focus were used. As an X-ray source, the Cu K line with a wavelength of 1.5406 is used. The usual range of 2 is 4-800. Each scan step is set at 0.8 seconds[86].

2.8 Fourier Transmission Infrared Spectroscopy (FTIR):

Infrared (IR) spectroscopy is the most often used spectroscopic method in both inorganic and organic chemistry for determining functional groups and the surface functionality of nanomaterials. Spectroscopy is the study of matter’s interaction with electromagnetic radiations (EMR). The energy of transmitted radiations is measured by the detector as the EMR of infrared wavelength (4000-400cm-1) travels through the sample[87].

Figure depicts the components of an FTIR equipment, which include a sample holding, detector, computer, and IR source. The glowing black body emits infrared radiations, which are allowed to flow through the aperture wherein the test sample is supplied a regulated quantity of energy. Certain frequency of molecular vibrations in the sample are absorbed, whereas the other frequencies are transmitted. As the beam approaches the detector, the typical IR spectra is recorded. The next thing to do is to digitalize the resulting signal and use a computer programme to execute the Fourier transform[88].

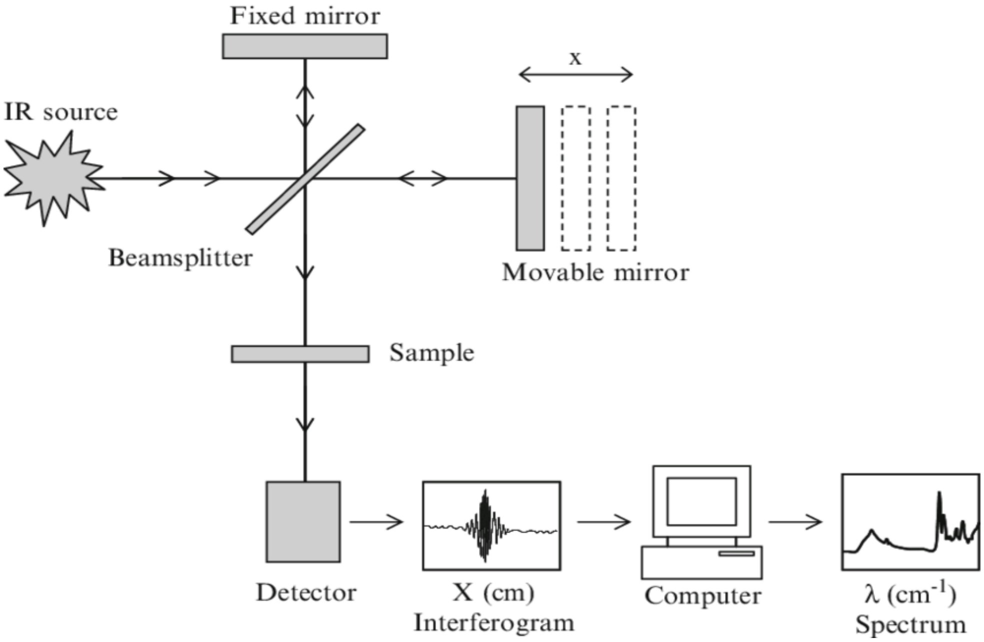

Figure 2.6: Schematic of FTIR Instrument [89]

IR was utilized in this study to identify the various functional groups contained in MOFs, including hydroxyl (OH), carbonyl (C=O), alkane (C-C), alkene (C=C), alkyne, carbon-nitrogen bond (C-N), amine (NH2) of organic linker, and metal bound oxygen (M-O). The atomic orbitals of both atoms overlap and merge to form molecular orbitals known as electronic orbitals. levels, which are subdivided into vibrational as well as rotational energy levels. If the molecule absorbs infrared light (400-4000 cm-1) and is stimulated by lower vibrational energy amounts to high levels of energy.

A covalent bond is formed when two atoms are connected by a hard connection, and every atom attracts an electron pair via nuclear pull. These nuclei shake as a result of bombardment radiations, and the oscillations are known as molecular vibrations. Only vibrations that stretch (symmetric and anti-symmetric) where atoms move back and forth are feasible in the case of a molecule that is diatomic (Figure Bending vibrations, in addition to stretching vibrations, are conceivable in polyatomic molecules.

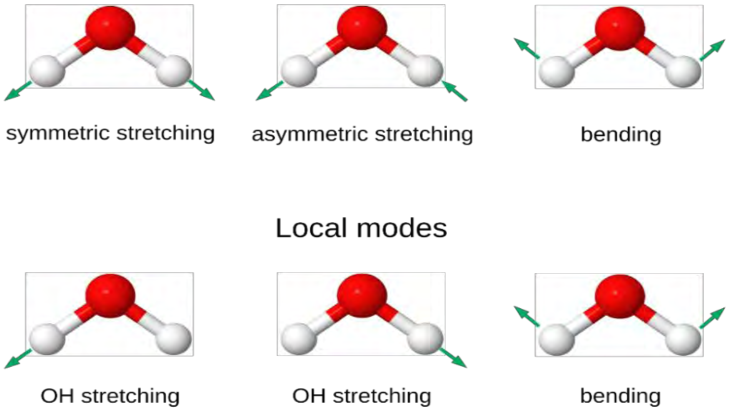

Figure 2.7: Stretching and bending modes of H_2O molecule.

The stretching frequency is connected to the masses of the bound atoms, but the bond strength has a connection to its force constant. The stretching frequency may be computed using the following formula:

$$\tilde{\upsilon} = 1/2\pi c \left(\frac{f(m1+m2)}{m1m2}\right)^{1/2}$$

Where ῦ is the frequency (cm-1), c is the velocity of light, f is force constant (Nm-1), and m1, m2 are the masses of two bonded atoms[90].

2.9 Scanning Electron Microscopy

SEM is a flexible method for studying the surface structure, texture, form, and size of materials at the nanoscale. The components of the SEM instrument are as follows: Vacuum, column, and an electron gun. In order to influence the sample during analysis, a primary electron beam (PEM) is fired into a high vacuum chamber using an electron cannon that has been vertically positioned and adjusted. By adjusting the applied voltage and electromagnetic lenses, the beam's energy and focusing may be adjusted, and its placement in relation to the sample can be controlled by adhering to a predetermined navigational framework. During PEM interactions with a material, electrons are scattered and generate signals in various directions. SEM analysis focuses on two types of electrons: SE and a few from deeper areas, BSE. SE electrons reveal surface roughness due to their high intensity and kinetic energy. When electrons collide with atomic nuclei, BSE electrons are formed, revealing information about the underlying material's atomic mass. These scattered electrons are detected by a through-lens detector. Conductive materials are ideal for SEM research because of electron collisions. Various conducting substrates are used, such as copper foil and carbon. Heavy metals like Pd, Pt, or Au are added to the surface to improve conductivity and contrast. All the samples were dry and in powder form, ready for inspection. Tiny amounts of powder, no more than 2mg, were put onto copper or alumina and any excess material was blown away before analysis [91].

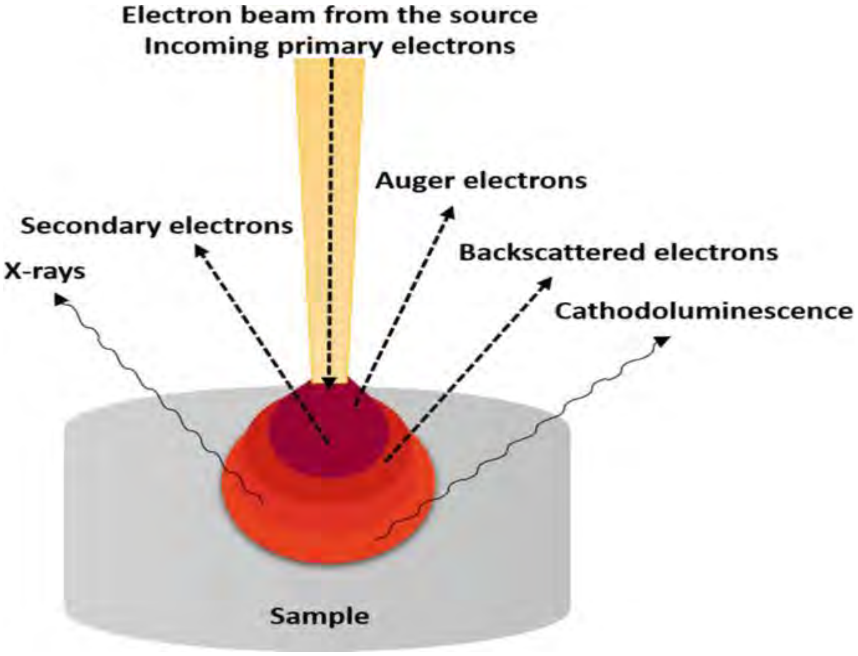

Figure 2.8: SEM working principle[92]

2.10 EDX Spectroscopy

By means of EDX scrutiny, the fundamental configuration of a substance can be unveiled. It is not an independent methodology; however, a scanning electron microscope is furnished with an additional X-ray receptor to amass X-ray emissions emitted from the interior of the specimen. The electron ray necessitates a noteworthy quantity of vigour to successfully infiltrate the essence whilst undertaking EDX exploration. When the electron ray meets the specimen, it causes openings by expelling electrons from the lower layers. Electrons from greater orbits shift to lower orbits to replenish these openings, exuding X-ray emissions in the course. The atomic load of the substance has a substantial influence on the vigor of these emissions focused on photomultiplier cylinders (PMTs). When exploited in combination with optical emitting material that may amplify the magnitude of photons exuded, the PTMs constitute an exceptionally susceptible sensor. By employing their associated X-rays, the diverse nuclei are discerned through this method, thereby facilitating the identification of the type of constituent as well as the quantification of the proportion of each element present throughout the entirety of the specimen. The scrutiny of the distribution of each element in the entire sample can be conducted using elemental mapping, which is based on this very principle. During this process, X-rays originating from various nuclei in the specimen manifest varying contrasts owing to their fluctuating atomic weights and % composition. The higher the energy of X-rays, the clearer the contrasts between elements, revealing their placement and uniformity. Atomic mass also increases with energy. Astoundingly, the identical protocol utilized for SEM investigation can be applied to both slender coatings and granular specimens. Nevertheless, to enliven an electron beam for the generation of X-rays throughout EDX scrutiny, a distinct receptor and a comparably elevated applied potential (20-30 kV) are implemented [93].

2.11 X-rays Photoelectron Spectroscopy (XPS)

To investigate surface properties, XPS is a versatile and useful method that can analyze chemical environment, electronic states, and material composition within a 10 nm range. It revolves on the photoelectric effect, in which the sample is hit by X-rays and emits photoelectrons in line with equation [94].

$$\textbf{Kinetic Energy} = h\nu - \textbf{Binding Energy} \ldots\ldots\ldots\ldots \textbf{(2.5)}$$

Photoelectrons' kinetic energy may be used to determine their binding energy. Electrons from the material's outermost layer and core level orbitals may be ejected during the interactions of rays (X-rays) with the specimen [95]. UPS is a technique that provides details on molecule bonding through surface electrons. It's named after the UV range's energy requirement for the outer orbital. However, in order to irradiate the specimen for XPS study, soft X-rays (200–2000 kV) must be produced since we are working with core level electrons. As a consequence of the expulsion of electrons from the innermost layer during excitation, vacancies are created. Figure 2.9 illustrates how electrons transition (from higher to lower orbital) to fill such vacancies by releasing energy as auger electrons or fluorescence. The location of the electron and the atomic number impact event likelihood. Auger electrons are more likely in lighter elements. Monochromatic radiations release electrons with varying kinetic energies. In the L and M shells, where electrons are more tightly bound and need more energy, they are released with less kinetic energy than those further from the nucleus. Electrons in circular path are detected with their kinetic energy. Only specific orbitals are used for XPS analysis. These orbitals are ideal for elements of different rows in periodic table. XPS assessment helps to analyze electrical state of each element. According to variations in their kinetic energy, electrons ejected from different orbitals are systematically collected by varying the applied voltage across the circular path. When photoelectrons or auger electrons come from a certain orbital, the detector can identify them and quantify their kinetic energy. Photoelectrons' kinetic energy, in contrast to auger electrons, is dependent on the X-ray source. It is extremely suggested to identify the source and provide the data as binding energy in order to obtain the proper fitting of the two peaks coming from each electron. When creating an ultra-high vacuum environment, a thin coating is used to prevent unwanted interaction. The sample is scanned to create peaks and then scanned again to analyze necessary elements. Data is processed and plotted against a standard to determine peak position. Selected samples are presented and labeled in each chapter.

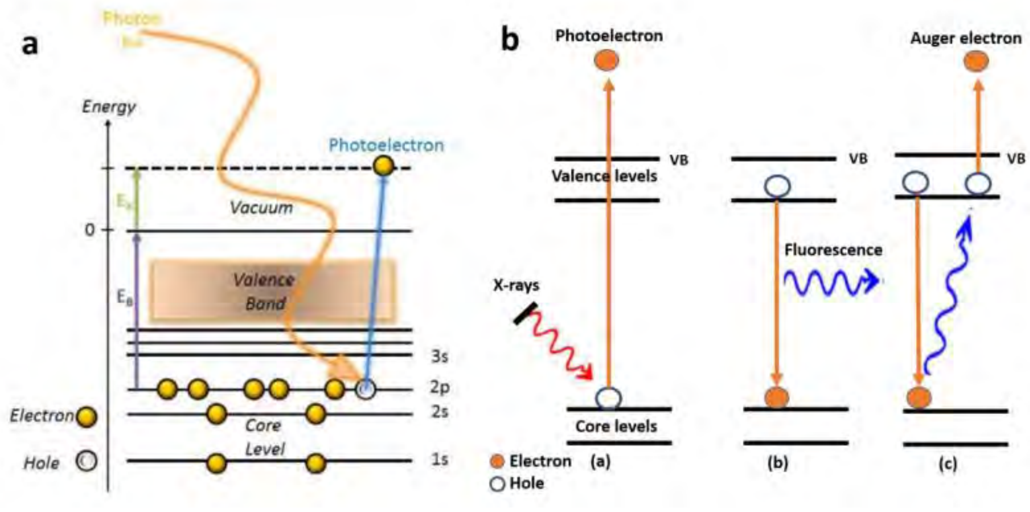

Figure 2.9: Photoelectric effect and electron creation (a) during the excitation and replenishment of vacancies (b) and (c) during photoelectron generation

2.12 Raman Analysis

The range of EMR used determines the obtained information. UV-visible spectra create electronic excitation for bonding info. Monochromatic radiation may not correlate to electronic excitation, forcing electrons to reach unstable energy level [96]. A potent monochromatic laser is used in Raman spectroscopy to interact with the sample, producing elastic and inelastic interactions. The primary component of the spectrum is the electrons returning to the same energy level, which is known as Rayleigh scattering.

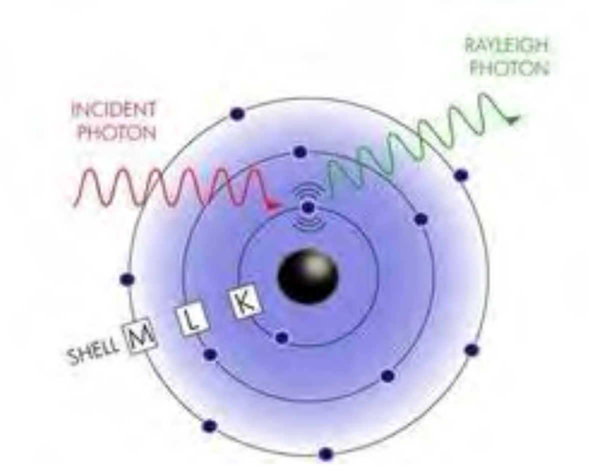

Figure 2.10: Rayleigh scattering

Only a few electrons lose energy during contact, resulting in excited vibrational levels near the ground electronic states. These electrons release photons with lower energy levels, known as the stokes component of the spectra. The return of a few electrons causes a more powerful photon release, known as 'anti-stokes'. This phenomenon, called the Raman effect, is represented by stokes and anti-stokes. Due to the electrons being more likely to be in the ground vibrational level, stokes is stronger than anti-stokes. This allows for high probability excitation/deexcitation. Therefore, we typically use the 'Stokes' reaction and graph it against dispersed photon intensity and frequency difference [97].

Raman spectroscopy has 25 varieties and is important for material research, especially 2D materials. It reveals flaws, deformation, amorphousness, and disturbance impact after chemical functionalization/doping. Eliminating/minimizing undesired Rayleigh lines is the main challenge during analysis. Parasitic radiation interferes with Stokes response.

Enchantment techniques like background elimination and monochromatic beam are needed. Sophisticated Raman spectroscopy techniques are used to increase photon intensity [98]. Not all motions in the material are Raman active. Light's interaction with matter results in a changed state. Raman effect produces quantum vibrational levels in crystal lattice. Molecules/lattices' charges disperse under magnetic field, but may form dipole. This behavior is inherent and may be anisotropic. The movements of molecules and crystal lattices create polarizability and dielectric susceptibility, which is the source of Raman activity. Only movements that generate polarizability are Raman active. This complements FT-IR spectroscopy, which only requires the dipole moment. Solid/powder samples were used for analysis, and the wavenumber versus the intensity of dispersed radiations was shown after removing background/fluorescence data [99].

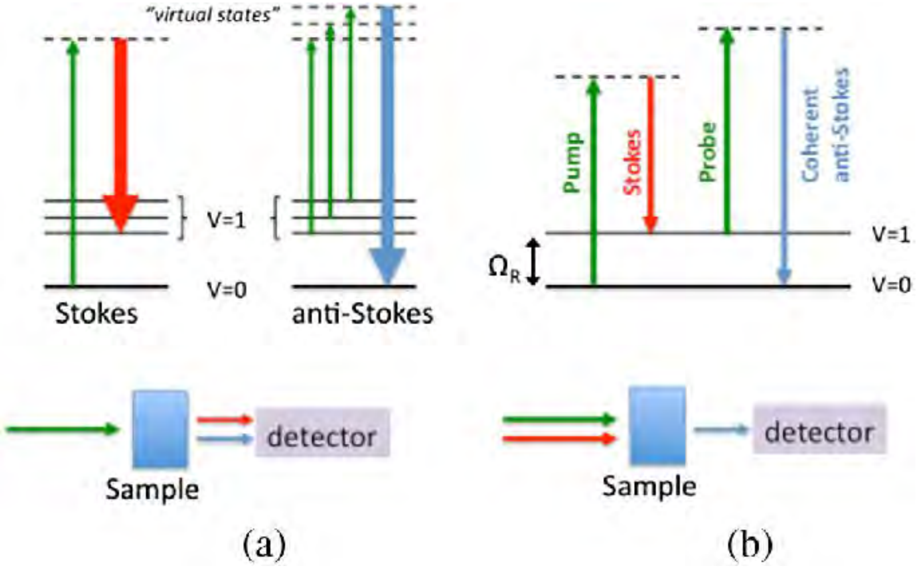

Figure 2.11: Principle of Raman scattering mechanisms[100]

2.13 Thermogravimetric Analysis

Thermogravimetric Analysis is an exquisite method that oversees the weight of a substance in correlation to temperature or time while exposing the specimen under examination to a well-regulated temperature program in a monitored milieu. Thermogravimetric Analysis is an exquisite method that oversees the weight of a substance in correlation to temperature or time while exposing the specimen under examination to a well-regulated temperature program in a monitored milieu. TGAs are available from PerkinElmer in two configurations: top-loading TGA 4000TM and bottom loading or hang down TGA 8000TM. A “stem” support rod on the TGA 4000 holds the specimen pan above the balance. The sample pan is supported by the TGA 8000 through a “hang down” below the balance. Both methods use gravity to generate extremely accurate and repeatable readings.

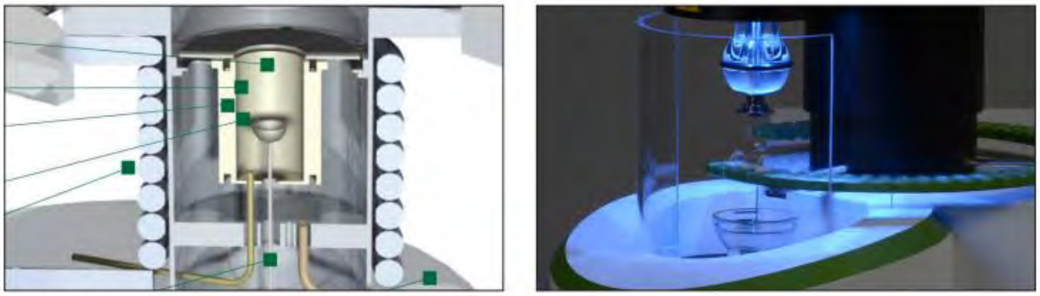
TGA 4000 TGA 8000

Figure 2.12: TGA Device

These devices can measure various types of losses and residues. They are usually used for heating but can also be used for cooling. The devices are managed by Pyris Software and have autosampler accessories for unattended operation. The TGA device includes a micro-furnace that may be quickly cooled. The heating component is composed of platinum and can withstand temperatures of up to 1,000°C. An exterior furnace containing a heating element constructed of a platinum-rhodium alloy may raise the temperature to 1,500°C.

A modern computer can calculate weight loss percentage. A commercial TGA can reach temperatures over 1,000°C and has a balancing sensitivity of 0.1 g. The heat-up rate in an air or gas environment can be adjusted from 0.1°C to 200°C/min [99].

The factors identified as affecting mass change include (1) the weight and volume of the specimen taken for analysis, (2) the physical form of the sample, (3) the shape and nature of the sample holder, (4) the nature of the surroundings in which the analysis takes place, (5) the pressure of the atmosphere kept in the chamber that holds the sample during the analysis, and (6) the rate of heating or cooling. Temperature fluctuations in sample mass are widely recognized. However, it is critical to recognize that not all sorts of thermal changes can impact the weight change of samples. TGA, for example, cannot be used to study sample melting and crystallization behavior.

CHAPTER 3

3. Results and Discussion

3.1 Phase and Structural Analysis of Different ZIF -7-I polymorph

3.1.1 ZIF-7-I

ZIF-7-I powder X-ray diffraction (XRD) patterns were obtained using a Bruker D8 X-ray diffractometer with Cu K (0.15415). ZIF-7-I is generated by bridging benzimidazolate (Bim) anions and zinc cations and has an open-framework structure. Figure 3.1 shows the prominent and recognizable peaks which shows the well define crystalline structure XRD of ZIF-7-I. The ZIF-7-I nano porous host structure allows for simple loading and unloading of guest molecules due to its flexible framework. A sharp characteristic diffraction doublet peaks at about 2θ=7.15° and 7.69° proves the efficacious creation of phase of ZIF-7-I[101]. The next diffraction peaks show the rhombohedral structure of ZIF-7-I[102]. The diffraction peaks at about 2θ=25.42°, 31.73°,34.38° and 36.20°indicates ZnO [101] All diffraction peaks in the ZIF-7 diffractogram appear at 2θ values of 7.15°, 7.69°, 12.11°, 12.36°, 15.43°, 16.25°, 18.29°, 19.50°, 21.07°, 22.97°, 25.41°, 26.50°, 27.79°, 31.73°,34.38°, 36.20° and can be indexed to reflections (101), (110), (021), (012), (030) (220), (031), (111), (121), (032), (-153), (-372)[103]. These peaks show ZIF-7 was successfully synthesized. The average particle size of synthesized ZIF-7-I was 15.686nm.

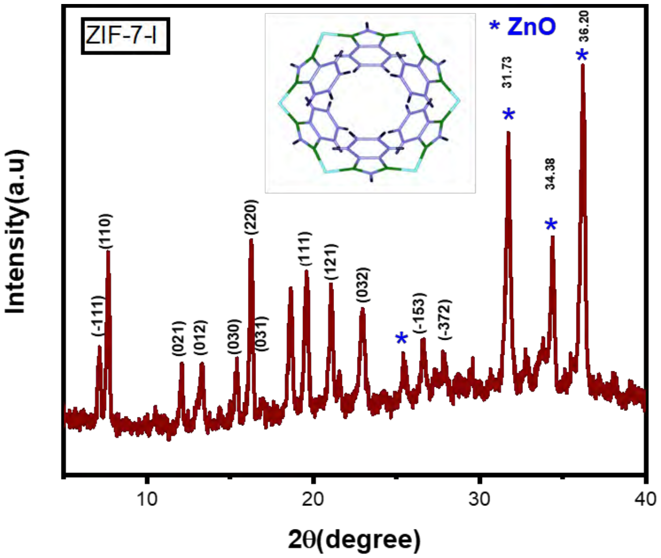

Figure 3.1: Structural Analysis of ZIF-7-I

3.1.2 ZIF-7-III/Zeolite

By adding 5wt% of zeolite there is phase shift from ZIF-7- I to ZIF-7 III. ZIF-7-III powder X-ray diffraction (XRD) patterns were obtained using a Bruker D8 X-ray diffractometer with Cu K (0.15415) radiation.ZIF-7-III, which is composed of zinc ions and benzimidazole (Bim). The structure of ZIF-7-III is classified as a dense lamellar phase, one of three phases of ZIF-7. Owing to its layered crystal structure, ZIF-7-III has attracted attention as a two-dimensional material. Each zinc ion is coordinated by four Bim ions to form a grid-like planar structure[104]. The diffraction peak at 2θ = 9.05° in the XRD pattern indicates the pure ZIF-7-III polymorph was obtained[105]. The diffraction peaks at about 2θ=27.38°,31.79°,34.44° and 36.20°indicates ZnO peaks. The diffraction peak at 2θ= 21.55° and 27.45° shows the presence of zeolite[106]. All diffraction peaks in the ZIF-7 diffractogram appear at 2θ values of 9.05°, 16.58°, 17.54°, 19.98°, 21.55°, 23.10°, 27.38°, 31.79°, 34.44°, 36.20°. The average particle size of synthesized ZIF-7-III was 60 nm.

Figure 3.2: Structural Analysis of ZIF-7-III

3.1.3 ZIF-7-I and ZIF-7-III

Figure3.3:Comparison of Structural Analysis of (a)ZIF-7-I (b) ZIF-7(I+III) (c) ZIF-7-III

The picture depicts the XRD of ZIF-7-I, ZIF-7-III, and a combination of ZIF-7(I+III). The figure depicts the distinct and recognizable peaks that demonstrate the well-defined crystalline structure. Figure (a) depicts the XRD of the ZIF-7-I. By adding 1.25wt% of zeolite in ZIF-7-I it is converted into a mixed phase containing the diffraction peaks of both ZIF-7-I and ZIF-7-III[57] as shown in the figure 3.3. And when the concentration of zeolite increases by 5wt% in ZIF-7-I it is converted to ZIF-7-III as shown in the figure3.2. All three phases contain the peaks of ZnO. The Prescence of zeolite can also be seen in the mixed phase of ZIF-7-I and ZIF-7-III and also in the ZIF-7-III phase[106].

3.2 Irradiation on ZIF-7-I

When the pure ZIF-7-I is exposed to lower ion beam radiation there is a phase shift in its structure from ZIF-7-I to ZIF-7-II.ZIF-7-II is known as narrow pore. This phase transition is from rhombohedral large pore phase to triclinic narrow pore phase[107]. The XRD pattern reveals that as the copper ions radiation increases, the intensity of the peak becomes more broadening. The peak position change towards lower two theta values indicate an expansion of the lattice, with significant changes in peak profiles and pronounced peak broadening at higher doses. The broadening is caused by an increase in the grain size and an increase in site dislocations, due to the similarity of Zinc and Copper ion's ionic radii. The lattice expands due to point and line defects, causing the XRD peaks to shift to lower two theta angles. As irradiation doses increase, there's a higher probability of creating defects and vacancies which lead to dislocation and interstitial loops. This causes peak broadening and gradual increase in macrostrain parameter. The diffraction peak at 16.231° and crystal plane at (021) on ZIF-7-I irradiated with copper ions created a defect and enhanced energy storage. On exposing the ZIF-7-I to radiations the guest molecules (DMF) present in ZIF-7 structure will be removed out and ZIF-7-II will be a guest free structure. The ZnO peaks present in ZIF-7-I structure as an impurity will also be removed. Notably, although the principal cavity for guest-hosting decreases in size from ZIF-7-I to ZIF-7-II, ZIF-7-II has a greater total volume along with void volume than a hypothetical model of ZIF-7-I without guest-hosting a guest or visitors.

Figure 3.4: Irradiated Structural Analysis of ZIF-7-II

3.3 Vibrational Mode analysis

3.3.1 ZIF-7-I

The Fourier Transform infrared (FTIR) spectra of ZIF-7-I is shown in the figure 3.5. The benzene ring's vibrations showed the most significant variations. All benzene rings in the ZIF-7-I phase are contained within spherical pores. The prominent feature observed in the spectra is sharp and well-define absorption band located at a wavenumber of 426cm^{-1}. This band can be described as Zn-N stretching vibration which serves as a definitive indicator of the presence of a chemical bond between the Zinc (Zn) ions and the Nitrogen(N) atom within the Benzimidazole ligand. The peaks 464, 557 and 655 cm^{-1} could be assigned to vibrations of C-C-C bonds in the benzene ring of the linker[59]. While the hydroxy phenyl benzimidazole (Bim) ligand's C-H bending vibration is visible at 740 cm^{-1}. [3.8] ZIF-7 reveals C-H out of plane bending at 775 and 905cm^{-1} from the Bim ligand and it also shows C-C-C trigonal bending at 1007cm^{-1}. ZIF-7-I phases show a double-peak in the region 1094, 1117, 1177 and 1203 cm^{-1} these peaks reveal the C-H in plane bending from Bim ligand. The peak at 1240 cm^{-1} is due to C-C stretching vibrations. The peaks at 1299 cm^{-1} and 1367 cm^{-1} shows the C-N stretching vibrations. The benzene ring's C=C stretching vibration is visible in the ZIF-7 at 1467cm^{-1} and1610cm^{-1} in the spectrum of the ZIF-7 phase is assigned to C=N bonds[59]. The peak at 1741 cm^{-1} gives N-H in plane bending + C-C-C out-of-plane bending.

Figure 3.5: Representation of illustrative peaks of ZIF-7-I

3..3.2 ZIF-7-I and ZIF-7-III/Zeolite

The figure shows the FTIR of ZIF-7 and ZIF-7-III.By adding 5wt% of zeolite as composite there is not much difference in the spectrum of ZIF-7-III.the FTIR spectrum of both ZIF-7-I and ZIF-7-III is same there is only stretching and vibrations of bonds. There is little change in its breathing mode and no breakage of bond is found[105].

Figure 3.6: Vibrational Spectroscopy (a) ZIF-7-I (b) ZIF-7-III

Table 3.1: FTIR peaks of ZIF-7-I and ZIF-7-III [105]

BANDS	**ZIF-7-I**	**ZIF-7-III**
Zn-N Bond	426cm^{-1}	426cm^{-1}
C-C-C bonds in the benzene ring	464-655cm^{-1}	468-649cm^{-1}
Hydroxy phenyl (Bim) ligand's	740cm^{-1}	740cm^{-1}
C-H out of plane bending	775-905cm^{-1}	775-905cm^{-1}
C-C-C trigonal bending	1007cm^{-1}	1007cm^{-1}
C-H in plane bending	1094-1203cm^{-1}	1091-1205cm^{-1}
C-C stretching	1240cm^{-1}	1242cm^{-1}
C-N stretching vibrations	1299-1367cm^{-1}	1367cm^{-1}
C=C stretching vibration	1467-1610cm^{-1}	1469-1610cm^{-1}
C=N bonds	1675cm^{-1}	1675cm^{-1}
N-H in plane bending + C-C-C out-of-plane bending.	1741cm^{-1}	1741cm^{-1}

3.4 Raman Vibrational spectroscopy

3.4.1 ZIF-7-I

The figure shows the Raman spectroscopy of pure ZIF-7-I. The peaks in Raman spectroscopy arise due to the Symmetric and asymmetric ring breathing, C-N stretching, and imidazole ring deformations cause the peaks. The first peak is round about 75cm^{-1} is due to light six-membered ring and four-membered rocking. The next peak at 154cm^{-1} shows the N-Zn-N bending (tetrahedral deformation) this is the major peak which shows the formation of MOFs. The peak at 547cm^{-1} shows Benzene and Imidazolate ring stretching. The next peak at 644cm^{-1} is due to Imidazolate ring torsion. The peak at 771cm^{-1} shows the Benzene and Imidazolate bending. Similarly, the peak at 1016cm^{-1} gives us the bending of benzene ring. C−H bending mode of benzene ring give rise to the next peak which is at 1113cm^{-1}. The peak at 1274cm^{-1} shows the Raman shift of imidazolate puckering bands and the C−H bending mode of the benzene ring. The peak at 1355cm^{-1} is due to stretching of C-N bond of the ligand imidazolate. The peak at 1575cm^{-1} shows the C-N stretching of benzimidazole. The peak at 3039 cm^{-1} shows C-H stretching of benzene ring. These are the major peaks in Raman spectroscopy [107].

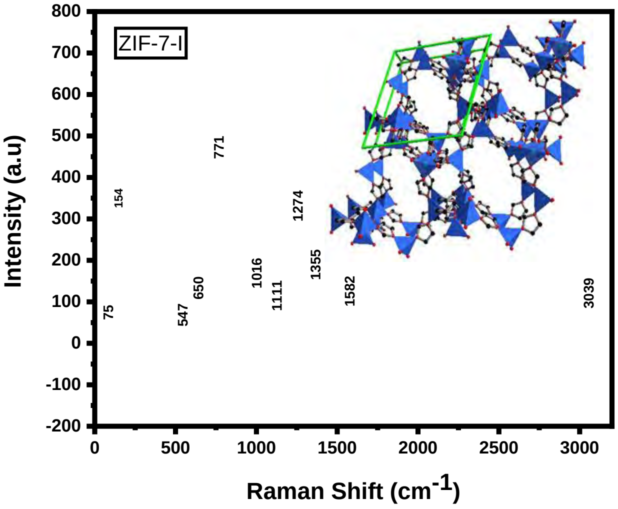

Figure 3.7: Inelastic Light scattering of ZIF-7-I

3.4.2 ZIF-7-I and ZIF-7-III

Several significant similarities between ZIF-7-I and ZIF-7-III were found in the comparable Raman spectroscopy research. Indicating the existence of consistent vibrational modes while structural components in both materials, both spectra showed shared peak positions and intensities. Additionally, there were no noticeable differences in the regions of interest between the ZIF-7-I and ZIF-7-III. Raman spectra which indicated overall spectral similarity. Importantly, the spectra of ZIF-7-III showed no new peaks that could be seen that weren't present in the entire spectrum of ZIF-7-I, suggesting that the substance's basic chemical groups and vibrational modes were preserved[107].

Figure 3.8: Inelastic Light Scattering (a) ZIF-7-I (b) ZIF-7-III

Table 3.2: The identification of the observed modes in the ZIF-7 and ZIF-7-III Raman spectra [107]

Pure ZIF-7-I	ZIF-7-III	Band Assignments
75	70	four-member and six-member rings
154	147	N−Zn−N bending (tetrahedral deformation)
547	530	Benzene and Imidazolate stretching
650	646	Imidazolate ring torsion
771	775	Benzene and Imidazolate bending
1016	1017	Benzene ring bending
1111	1109	C−H bending
1274	1274	Imidazole X−H and Benzene C−H (symmetric) bending
1355	1356	Imidazolate C−N stretching
1582	1578	N−H bending
3039	3034	Benzene C−H stretching

3.5 High Resolution Electron Microscopy

3.5.1 ZIF-7-I

SEM was used to examine the surface morphology of the prepared sample. The as-synthesized ZIF-7-I SEM picture (Figure 3.9) displays homogeneous nanometer-sized spherical crystals consisting of smaller irregular particles. When compared to those reported in the literature. ZIF-7-I particles do not have well-defined crystal faces and agglomerated, which is most likely due to the rapid deprotonation rate of organic ligands in water/ethanol ammonium hydroxide solution, leading to crystal growth in all directions and larger crystals[101][108]. ZIF-7-I contained a number of elements as shown by the EDX spectrum that was obtained after the analysis of sample. The most prominent elements discovered are listed in the table along with their corresponding atomic percentages.

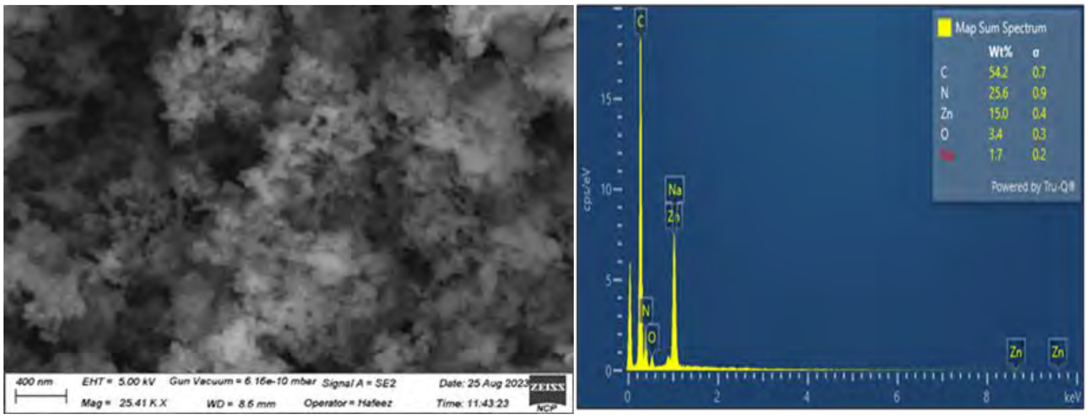

Figure 3.9: High Resolution Image and EDX of pure ZIF-7-I

Table 3.3: EDX acquired for ZIF-7-I

Elements	Weight%	ϭ
C	54.2	0.7
N	25.6	0.9
Zn	15.0	0.4
O	3.4	0.3

Figure depicts the morphology of ZIF-7-III. Zeolites, with their unique crystalline characteristics, may improve contrast in SEM pictures, allowing for better visualization of the arrangement and shape within the composite. ZIF-7-I is an insulator because it contains organic ligands that are non-polar and are insulators. Furthermore, Zeolite is also non polar and both ZIF-7-I and Zeolite have insulating properties, subjecting the composite to surface charge during imaging. The zeolite will be evenly dispersed throughout the ZIF-7 matrix as it is shown in the figure[104].

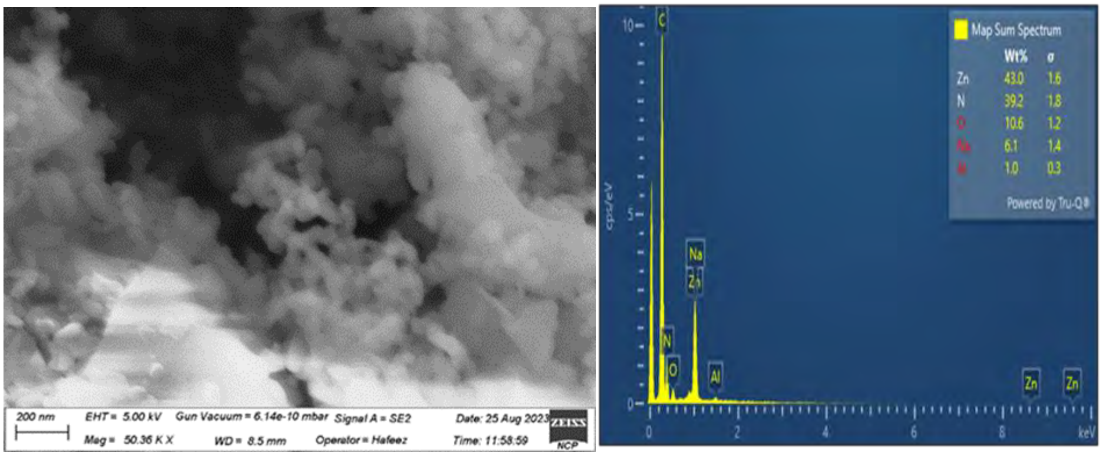

Figure 3.10: High Resolution Image of ZIF-7-III with Zeolite

Table 3.4: Prominent Elements during EDX of ZIF-7-III

Elements	Weight%	σ
N	39.2	1.8
Zn	43	1.6
O	10.6	1.2
Al	1.0	0.3

3.6 X-ray Photoelectron Spectroscopy

As a crucial characteristic method to identify the chemical states of various species in the pure ZIF-7-I, X-ray photoelectron spectroscopic analysis has been used. The XPS spectrum reveals the elements present and their corresponding binding energies. The findings of the acquired XPS characterization show that ZIF-7's composite structure has been successfully constructed. The XPS survey spectrum of ZIF-7-I pure exhibits peaks for carbon, nitrogen, oxygen, and zinc, as seen in Figure 1(S1). Additionally, these elements satisfy the description of the elemental composition given by EDS. These elements' binding energies reflect the chemical states in which they exist in the substance[104].

Figure 3.11: XPS spectrum of ZIF-7-I (S1) survey spectrum

As a crucial characteristic method to identify the chemical states of various species in the pure ZIF-7, X-ray photoelectron spectroscopic analysis has been used. The XPS spectrum reveals the elements present and their corresponding binding energies. The findings of the acquired XPS characterization show that ZIF-7's composite structure has been successfully constructed. The XPS survey spectrum of ZIF-7 pure exhibits peaks for carbon, nitrogen, oxygen, and zinc, as seen in Figure 1(S1). Additionally, these elements satisfy the description of the elemental composition given by EDS. These elements' binding energies reflect the chemical states in which they exist in the substance. For the C1s area, shown in (S2), the carbon peak appears about 285 eV. The carbon atoms that make up the material's organic structure are represented by this peak. The binding energy for the C 1 s peak at 285 eV was used as the calibration reference because the C element could be attributed to the incidental carbon-based contamination. Around 399 eV, the nitrogen peak in the N1s region, Figure 1(S3), is seen. The nitrogen atoms of the ligand are reflected in this peak. Around 532 eV, the oxygen peak, Figure 1(S4), in the O1s area can be seen. The oxygen atoms in both the ligand and this peak are represented by this peak. The presence of the zinc $2p_{1/2}$ and $2p_{3/2}$ peaks, Figure 1(S5), at 1044 and 1021 eV, respectively, demonstrate the divalent Zn element in the synthesized material[109]. The zinc ions are coordinated with the ligand because there is a trace amount of zinc in the formula. The oxidation state and coordination environment of the zinc ions within the framework affect the binding energy of the zinc peak. Overall, ZIF-7's elemental composition and the chemical states of these elements are revealed by XPS analysis, shedding light on the material's structure and elemental makeup.

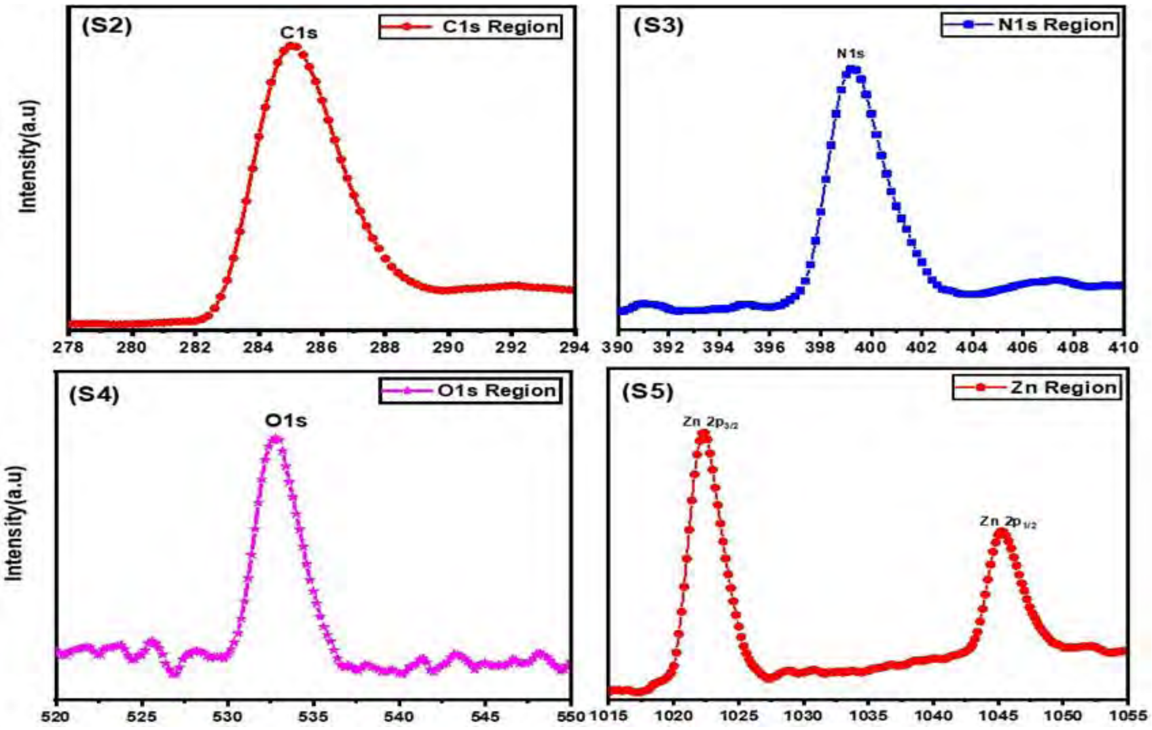

Figure 3.12: XPS spectrum of C1s spectrum (S2), N1s spectrum (S3), O1s spectrum (S4), and Zn 2p (S5) spectrum.

Table 3.5: Percentage of elements during XPS

Peak ID	Atomic%	Binding Energy (BE)
Zn 2p3/2	3.00%	1022.2
N 1s	78.90%	399.2
C 1s	78.90%	285
O1s	9.10%	532

3.7 Thermogravimetric Analysis

3.7.1 ZIF-7-I and ZIF-7-III

Thermogravimetric Analysis (TGA) is a technique used to determine the changes in a materials weight as it is heated or cooled.it tells us about materials thermal stability, decomposition temperature and amount of weight loss and gained during heating providing insights into its composition decomposition kinetics and potential applications.

Figure 3.13: Thermal Decomposition Analysis of Polymorphs of ZIF-7-I

Finally, TGA of ZIFs was carried out in a N_2 environment as shown in figure. The sample was heated to a maximum of 1200°C, starting from ambient temperatures.ZIF-7-I was thermally stable at temperatures as high as 540 °C. Below 260 °C all the solvents, unreacted species and guest molecules were removed. After 550 °C ZIF-7-I will be less thermally stable and bond breakage will start. This is the point at which material shows thermal decomposition [110].

ZIF-7-III undergoes two step thermal decay. Around 220°C, the material starts to lose weight all solvents, unreacted species and guest molecules evaporate out. It is the temperature at which ZIF-7-III begins to thermally decompose is denoted by this point. Around 565°C, the curve completely flattens out. This temperature corresponds to the point at which the material has fully decomposed thermally it cannot be stable after this temperature[111].

3.8 Linear Current Voltage (LCV) Analysis

To explore the OER activity of pure ZIF-7 electrocatalyst, LSV was performed using the Gamry Interface 1010e galvanostat/potentiostat in the potential range of 0 to 0.8 V vs.RHE in 1M KOH solution at a scan rate of 5mV/s in three electrode system in which platinum wire was counter electrode and Ag/AgCl was reference electrode and various Polymorphs of ZIF-7-I was working electrode was of 1×1 cm^2 dimension. All measured potential values were converted to RHE using the formula ERHE = EAg/AgCl + 0.197 + 0.059 × pH, where pH of the solution was 14 that was used in water oxidation. Electrode potential was measured at a current density of $10mAcm^{-2}$ to investigate the OER performances of modified electrodes. The OER tests was performed on Nickle foam for each electrocatalyst under similar conditions. The slow OER process at low overpotential is only promoted by the encouragement of intrinsic catalytic behavior to readily enable the 4 electrons transfer process that occurs among the catalyst's surface and the adsorbed species. Tafel plots were derived from the corresponding LSV curves by plotting overpotential (η) vs.log j in accordance with the equation

$$\eta = a + b\log (j)$$

where η is overpotential, b is Tafel slope, j is current density, and a is exchange current density.

3.8.1 ZIF-7-I

LSV test of ZIF-7-I was performed in 1M KOH solution to evaluate the electrocatalytic oxidation activities. The synthesized electrodes were electrochemically evaluated using linear sweep voltammetry in the range from 0 to 1.8 V versus RHE at a 5 mV/s scan rate. The electrode potential was measured to be 1.644V generating an overpotential of 414mV to achieve the current density of 10 $mAcm^{-2}$. Through the use of the Tafel slope, electrochemical performance for OER was further examined in terms of kinetics and the value of Tafel slope was calculated 66.98mV/dec by plotting overpotential (η)vs.log j[112].

Figure 3.14: (a) LSV curve of ZIF-7-I (b) Tafel plot for ZIF-7-I

3.8.2 ZIF-7-(I+III)

LSV test was performed in 1M KOH solution to evaluate the electrocatalytic oxidation activities. The synthesized electrodes of area 1*1 were electrochemically evaluated using linear sweep voltammetry at a 5 mV/s scan rate in the range of 0 to 1.8 V versus RHE. The electrode potential was measured to be 1.52056V generating an overpotential of 290mV to achieve the current density of 10 mAcm^{-2}. Tafel slope was calculated 59.21mV/dec by plotting overpotential (ɳ) vs.log j.

Figure 3.15: (a) LSV curve of ZIF-7-I & III (b) Tafel plot for ZIF-7-I & III

Addition of 0.25wt% of zeolite in pure ZIF-7-I enhance the catalytic activity for water oxidation and lowering the value of overpotential as compared to pure ZIF-7-I for water oxidation. This is because zeolite have active sites on its surface and addition of zeolite introduce additional active sites which helps to improve the catalytic activity. Zeolite may further enhance the ZIF-7-I framework's stability and endurance, ensuring long-term catalytic efficacy.

3.8.3 ZIF-7-III

LSV test of ZIF-7-III was performed in 1M KOH solution to evaluate the electrocatalytic oxidation activities. The synthesized electrodes of area 1*1 were electrochemically evaluated using linear sweep voltammetry at a 5 mV/s scan rate in the range of 0 to 1.8 V versus RHE. The electrode potential was measured to be 1.6174V generating an overpotential of 387mV to achieve the current density of 10 mAcm-2. Tafel slope was calculated 48.49mV/dec by plotting overpotential (ƞ) vs.log j. Addition of 5wt% of zeolite in ZIF-7-I enhance the catalytic activity but when the concentration of zeolite increases, an unexpected phenomenon arises, in which the overpotential value begins to climb rather than decrease as predicted. This behavior is the result of a complicated interaction of causes. There may be an ideal zeolite concentration that improves catalytic activity by adding new active sites or altering the local environment in a favorable way. Beyond this limit, an excess of zeolite might potentially impede or interfere with the ZIF-7 framework's active sites and catalytic activity of some impurities may also occur which causes an increase in the value of overpotential[105].

Figure 3.16: (a) LSV curve of ZIF-7-III (b) Tafel plot for ZIF-7-III

3.8.4 Pure Zeolite

LSV test of pure zeolite was performed in 1M KOH solution to evaluate the electrocatalytic oxidation activities. The synthesized electrodes were electrochemically evaluated using linear sweep voltammetry at a 5 mV/s scan rate in the range of 0 to 1.8 V versus RHE. The electrode potential was measured to be 1.715V generating an overpotential of 485mV to achieve the current density of 10 mAcm^{-2}. Tafel slope was calculated 154.mV/dec by plotting overpotential (ɳ) vs.log j

Figure 3.17: (a) LSV curve of Pure Zeolite (b) Tafel plot for Pure Zeolite

The value of overpotential as well as the value of Tafel plot of pure Zeolite is quite high but when it gets mixed with ZIFs it gives us remarkable values.

3.8.5 Comparative LSV analysis

To examine the OER activity of synthesized electrodes LSV was performed in 1M KOH. The overpotential of pure sample ZIF-7-I was 414 mV at 10mAcm^{-2} and value of Tafel slope is 66.98mV /dec but on the addition of zeolite the value of overpotential was decreased. The overpotential of combination of ZIF-7-(I+III) was 290mV and the value of Tafel slope was 59.21mV/dec. Whereas, the value of overpotential of ZIF-7-III was 387mV and the value of Tafel slope was 48.49mV/dec. Tafel slope shows the kinetics of our sample Lower the value of Tafel slope higher will be the kinetics and better will be the performance. From above comparison we can see that the Tafel slope value of ZIF-7-III is lower which shows higher kinetics and due to higher kinetics in ZIF-7-III and more active sites catalytic activity of unwanted particles also increases which causes the increase in the value of overpotential.

Figure 3.18: Comparative LSV analysis

We can see on the addition of Zeolite as composite in pure ZIF-7-I the value of overpotential decreases and Tafel value slope increases. There is a fixed ratio of zeolite which should be added in the sample as composite above that ratio the value of overpotential may increase due to excess of active sites. The results for 2.5wt% of zeolite and 5wt% zeolite in pure sample was same. The results obtained by the addition of 1.25wt% of zeolite are the best among all. From this we can say that combination of ZIF-7(I+III) is the best electrocatalyst to evaluate oxygen. In case of pure Zeolite, the value of overpotential is 485mV and the value of Tafel slope is 154.76mV/dec. In case of pure zeolite both the values are high but when it gets merge with ZIF-7-I its value for overpotential decreases and value to Tafel slope also gets better. Combination of zeolite with ZIFs create good electrocatalyst for Oxygen evolution.

3.9 Electrochemical Impedance Spectroscopy

The strong OER activity of the was analyzed mechanistically using electrochemical impedance spectroscopy. The width of the semicircle in the high frequency region reveals the charge-transfer resistance for electrocatalysts, demonstrating electron-transfer kinetics at the electrode interface, and the positive portion of impedance was plotted against its imaginary part in the Nyquist plot. A wider semicircle was seen in the case of ZIF-7-I, which pointed to delayed electron transfer for OER and high charge-transfer resistance. The solution resistance lies in the place from where the semi- circle starts in case of ZIF-7-I it is higher as compared to composites. The Electro Chemical impedance of ZIF -7-I is maximum showing high charge transfer resistance and low catalytic activity when compared to combination of ZIF-7(I+III) and ZIF-7-III [113].

Figure 3.19: Electrochemical impedance spectroscopic measurements

A smaller semicircle was seen in the case of combination of ZIF-7-(I+III), this is due to 1.25wt% addition of zeolite which pointed to fast electron transfer for OER and low charge-transfer resistance. ZIF-7-(I+III) electrochemical activity is at its maximum in its smallest semicircle. The solution resistance of ZIF-7-(I+III) is very less as compared to others. In case of ZIF-7-III a large semi-circle is seen but it is smaller as compared to ZIF-7-I and larger as compared to combination ZIF-7- (I + III). This is due to 5wt% addition of zeolite. When the concentration of zeolite increases surface porosity of ZIF-7-III also increases which leads to higher charge transfer resistance and low catalytic activity even due to which electrochemical activity become little bit less. The solution resistance for ZIF-7-III is same as compared to solution resistance of ZIF-7-I[114]

3.10 Chronoamperometry

Chronoamperometric investigations demonstrated the stability of all ZIF-7-I polymorphs when tested for 15 hours of continuous oxygen production.

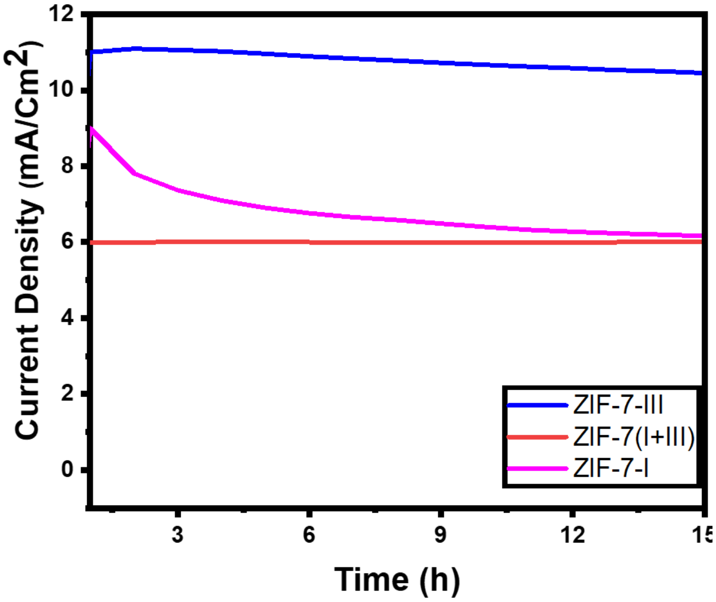

Figure 3.20: Chronoamperometry for various Polymorphs of ZIF-7-I

The ZIF-7(I+III) electrocatalyst was dipped in 1M KOH solution of area $1*1cm^{-2}$ and left overnight for 15 hours to measure its stability test. The straight line shows that the combination of ZIF-7(I+III) was highly stable. The electrocatalyst did not leech out during this whole process showing its stability. ZIF-7-III and it is less stable than ZIF-7(I+III).

Table 3.6: Comparison of different polymorphs

Techniques	ZIF-7-I	ZIF-7 (I+III)	ZIF-7-III
LSV	414mV	290mV	387mV
EIS	Wider semi-circle	Smaller semi-circle	Wider semi-circle
Tafel Slope	66.98mV/dec	59.21mV/dec	48.49mV/dec
Chronoamperometry	Stable	Outstanding	Stable

From the table we can see the electrochemical techniques we have performed for water splitting for oxygen evaluation reaction. The best values for all techniques are of ZIF-7 (I+III) which shows it is the best electrocatalyst for oxygen evaluation. This electrocatalyst is formed by 1.25wt% addition of zeolite in pure ZIF-7-I. OER is the $4e^-$ multistep process that requires 240-600 mV of additional energy, making it both kinetically as well as thermodynamically unfavorable. Efforts have been made to speed up the kinetics of the water-splitting process at a potential (1.23 V) that is near to the thermodynamic limits. Our electrocatalyst ZIF-7 (I+III) need 290 mV of additional energy to evaluate oxygen and it is very near to standard value which shows this electrocatalyst is very remarkable to evaluate oxygen which can be further use in fuel cells and metal air batteries.

ZIF-7 (I+III) also have a very good catalytic activity which shows charge transfer is also great. The value of Tafel Slope was also less and smaller value shows better kinetics. Chronoamperometry tell us about the stability and the straight line shows that it is highly stable.ZIF-7 (I+III) is stable for 15 hours making it an efficient candidate for water splitting for the evaluation of oxygen.

4. Conclusion

Since the last few decades, as energy demands have increased, scientists have focused on developing renewable power sources that are more environmentally friendly than fossil fuels. As they are not environmentally friendly energy sources that also cause ecological contamination, fossil fuels are becoming more and more scarce with the expanding population and industrialization. Water serves as the vital medium to store energy an effective electrocatalyst has been created to split the water in order to store energy. This electrocatalyst will be utilized to produce oxygen, which is a necessary step in the production of clean energy for fuel cells. In our investigation, three different polymorphs were designed and zeolite was used as a composite. The three phases of ZIF-7 are described as ZIF-7-I, ZIF-7(I+III) and ZIF-7-III with a space group of rhombohedral(R-3), triclinic(P-1) and monoclinic(C2/c) respectively. ZIF-7 (I) is prepared from Zinc nitrate as metal nodes and benzimidazole as a linker, that crystallizes in the rhombohedral conformation with a lattice parameter of a=22.989[Å] b=22.989[Å] c=15.763[Å]. We further found that on addition of 1.25wt% of zeolite to pure ZIF-7(I) phase there triggers a phase transformation to ZIF(III) polymorph and we ended up into a combination of ZIF-7 (I+III) mixture. When the concentration of Zeolite increases to 5wt% into pure ZIF-7-I it is completely transformed into ZIF-7-III phase that crystallizes in the space group monoclinic (C2/c) with a lattice parameter of a= 16.106A b=19.511Å c=16.126Å. ZIF-7-I is further irradiated with 500 keV (Cu++) ions at dosages of 1×10^{14} ions cm^{-2}that causes yet another stimulating phase transformation from ZIF-7-I to a less symmetric ZIF-7-II polymorph that crystallizes in the space group triclinic (P-1) with a lattice parameter of a=23.984[Å] b=21.354[Å] c=16.349Å.This comprehensive study integrated a variety of analytical techniques, such as XRD for phase identification, phase transformation from ZIF-7-I(rhombohedral) with a space group of R-3 to ZIF-7-III (monoclinic) with a space group of C2/c and crystal size determination that was 15.686nm. The FTIR spectra of different polymorphs of ZIF-7 samples display the characteristics vibrational and stretching modes along with the formation of major bond at 426cm-1 attributed to Zn-N stretching modes that affirm the connectivity of metal nodes of Zn with benzimidazole linkers a vital part for the formation of porous framework. SEM was used for surface morphology inspection and the particle morphology of ZIF-7-I was circular and average particle size was 61.30nm, Raman spectroscopy was used for mode identification and major mode was of Zn-N bond at 154cm^{-1}, XPS was used to determine elemental composition the main elements were C, N, O and Zn. TGA was used for thermal stability assessment ZF-7-I was stable up to 540 C and ZIF-7-III was stable up to 560℃. A suite of electrochemical techniques, such as EIS to probe charge transfer resistance LSV to find the value of overpotential Tafel slope to find the kinetics and chronoamperometry to find stability of material. The over potential value of pure ZIF-7-I was 414mv at 10cm-2 and have a wide semi-circle in EIS. When 1.25wt% of zeolite was added in pure ZIF-7-I it transforms into a mixture of ZIF-7(I+III) the value of overpotential decreases and the area of semi-circle also decreases which shows low charge transfer resistance and high catalytic activity than pure ZIF-7-I.the value of Tafel slope also increases that is 59.21mV/dec this shows the higher kinetics of particles. When 5wt% of zeolite is added in pure ZIF-7-I it transforms from ZIF-7-I to ZIF-7-III. The value of overpotential of ZIF-7-III is 387mV and area of semi-circle is small as compared to pure ZIF-7-I and large as compared to the mixture of ZIF-7 (I+III) which shows high charge transfer resistance and low catalytic activity. This is because ZIF and Zeolite both are porous when the concentration of zeolite increases porosity of ZIF-7-III increases leading to the catalytic activity of unwanted particles which increases the value of overpotential. Through these thorough examinations, we have seen the significant influence that zeolite incorporation had on the polymorph structure. A hierarchically porous electrocatalyst with higher electrochemical performance is produced as a result of the transformation from ZIF-7-I to ZIF-7-III by zeolite integration. The best electrocatalyst for water splitting was combination of ZIF-7 (I+III) whose overpotential value is 290mV which is very near to standard. These results provide a compelling path for the clean and efficient conversion of energy, holding significant potential for the development of fuel cell technology and sustainable energy generation. However, this journey is still ongoing, and additional research is necessary to improve the composite material as well as investigate its possibilities in real-world applications, paving the way for a more environmentally friendly and sustainable energy future.

References

[1] Y. Chang, A. Braun, A. Deangelis, J. Kaneshiro, and N. Gaillard, “Effect of thermal treatment on the crystallographic, surface energetics, and photoelectrochemical properties of reactively cosputtered copper tungstate for water splitting,” *J. Phys. Chem. C*, vol. 115, no. 51, pp. 25490–25495, 2011, doi: 10.1021/jp207341v.

[2] M. Amin *et al.*, “Hydrogen production through renewable and non-renewable energy processes and their impact on climate change,” *Int. J. Hydrogen Energy*, vol. 47, no. 77, pp. 33112–33134, 2022, doi: 10.1016/j.ijhydene.2022.07.172.

[3] J. Fiksel, “Sustainability and resilience: toward a systems approach,” *Sustain. Sci. Pract. Policy*, vol. 2, no. 2, pp. 14–21, 2006, doi: 10.1080/15487733.2006.11907980.

[4] C. D. Korkas, S. Baldi, I. Michailidis, and E. B. Kosmatopoulos, “Occupancy-based demand response and thermal comfort optimization in microgrids with renewable energy sources and energy storage,” *Appl. Energy*, vol. 163, pp. 93–104, 2016, doi: 10.1016/j.apenergy.2015.10.140.

[5] M. M. Vanegas Cantarero, “Of renewable energy, energy democracy, and sustainable development: A roadmap to accelerate the energy transition in developing countries,” *Energy Res. Soc. Sci.*, vol. 70, 2020, doi: 10.1016/j.erss.2020.101716.

[6] W. Fuqiang, C. Ziming, T. Jianyu, Y. Yuan, S. Yong, and L. Linhua, “Progress in concentrated solar power technology with parabolic trough collector system: A comprehensive review,” *Renew. Sustain. Energy Rev.*, vol. 79, pp. 1314–1328, 2017, doi: 10.1016/j.rser.2017.05.174.

[7] C. L. Muhich, B. D. Ehrhart, I. Al-Shankiti, B. J. Ward, C. B. Musgrave, and A. W. Weimer, “A review and perspective of efficient hydrogen generation via solar thermal water splitting,” *Wiley Interdiscip. Rev. Energy Environ.*, vol. 5, no. 3, pp. 261–287, 2016, doi: 10.1002/wene.174.

[8] O. Ellabban, H. Abu-Rub, and F. Blaabjerg, “Renewable energy resources: Current status, future prospects and their enabling technology,” *Renew. Sustain. Energy Rev.*, vol. 39, pp. 748–764, 2014, doi: 10.1016/j.rser.2014.07.113.

[9] S. Y. Tee *et al.*, “Recent Progress in Energy-Driven Water Splitting,” *Adv. Sci.*, vol. 4, no. 5, 2017, doi: 10.1002/advs.201600337.

[10] A. Buttler and H. Spliethoff, “Current status of water electrolysis for energy storage, grid balancing and sector coupling via power-to-gas and power-to-liquids: A review,” *Renew. Sustain. Energy Rev.*, vol. 82, pp. 2440–2454, 2018, doi: 10.1016/j.rser.2017.09.003.

[11] Y. He, T. Hamann, and D. Wang, “Thin film photoelectrodes for solar water splitting,” *Chem. Soc. Rev.*, vol. 48, no. 7, pp. 2182–2215, 2019, doi: 10.1039/c8cs00868j.

[12] S. Wang, A. Lu, and C. J. Zhong, “Hydrogen production from water electrolysis: role of catalysts,” *Nano Converg.*, vol. 8, no. 1, 2021, doi: 10.1186/s40580-021-00254-x.

[13] I. Roger, M. A. Shipman, and M. D. Symes, “Earth-abundant catalysts for electrochemical and photoelectrochemical water splitting,” *Nat. Rev. Chem.*, vol. 1, 2017, doi: 10.1038/s41570-016-0003.

[14] M. Mahmoud, M. Ramadan, A. G. Olabi, K. Pullen, and S. Naher, “A review of mechanical energy storage systems combined with wind and solar applications,” *Energy Convers. Manag.*, vol. 210, 2020, doi: 10.1016/j.enconman.2020.112670.

[15] J. D. Holladay, J. Hu, D. L. King, and Y. Wang, “An overview of hydrogen production technologies,” *Catal. Today*, vol. 139, no. 4, pp. 244–260, 2009, doi: 10.1016/j.cattod.2008.08.039.

[16] K. M. Abraham, “Prospects and limits of energy storage in batteries,” *J. Phys. Chem. Lett.*, vol. 6, no. 5, pp. 830–844, 2015, doi: 10.1021/jz5026273.

[17] S. Li *et al.*, “Designing interfacial chemical bonds towards advanced metal-based energy-storage/conversion materials,” *Energy Storage Mater.*, vol. 32, pp. 477–

496, 2020, doi: 10.1016/j.ensm.2020.07.023.

[18] S. Ardo *et al.*, “Pathways to electrochemical solar-hydrogen technologies,” *Energy Environ. Sci.*, vol. 11, no. 10, pp. 2768–2783, 2018, doi: 10.1039/c7ee03639f.

[19] N. Zaman, T. Noor, and N. Iqbal, “Recent advances in the metal-organic framework-based electrocatalysts for the hydrogen evolution reaction in water splitting: a review,” *RSC Adv.*, vol. 11, no. 36, pp. 21904–21925, 2021, doi: 10.1039/d1ra02240g.

[20] S. S. Mukrimaa *et al.*, “No 主観的健康感を中心とした在宅高齢者における 健康関連指標に関する共分散構造分析Title,” *J. Penelit. Pendidik. Guru Sekol. Dasar*, vol. 6, no. August, p. 128, 2016.

[21] A. Phan, C. J. Doonan, F. J. Uribe-Romo, C. B. Knobler, M. Okeeffe, and O. M. Yaghi, “Synthesis, structure, and carbon dioxide capture properties of zeolitic imidazolate frameworks,” *Acc. Chem. Res.*, vol. 43, no. 1, pp. 58–67, 2010, doi: 10.1021/ar900116g.

[22] Y. S. Bae, A. Ö. Yazayd’n, and R. Q. Snurr, “Evaluation of the BET method for determining surface areas of MOFs and zeolites that contain Ultra-Micropores,” *Langmuir*, vol. 26, no. 8, pp. 5475–5483, 2010, doi: 10.1021/la100449z.

[23] X. C. Huang, Y. Y. Lin, J. P. Zhang, and X. M. Chen, “Ligand-directed strategy for zeolite-type metal-organic frameworks: Zinc(II) imidazolates with unusual zeolitic topologies,” *Angew. Chemie - Int. Ed.*, vol. 45, no. 10, pp. 1557–1559, 2006, doi: 10.1002/anie.200503778.

[24] P. Garrido-Barros, J. Derosa, M. J. Chalkley, and J. C. Peters, “Tandem electrocatalytic N2 fixation via proton-coupled electron transfer,” *Nature*, vol. 609, no. 7925, pp. 71–76, 2022, doi: 10.1038/s41586-022-05011-6.

[25] Q. Mou *et al.*, “A bimetal hierarchical layer structure MOF grown on Ni foam as a bifunctional catalyst for the OER and HER,” *Inorg. Chem. Front.*, vol. 8, no. 11, pp. 2889–2899, 2021, doi: 10.1039/d1qi00267h.

[26] F. Zhang, Y. Zhu, Q. Lin, L. Zhang, X. Zhang, and H. Wang, “Noble-metal single-atoms in thermocatalysis, electrocatalysis, and photocatalysis,” *Energy Environ. Sci.*, vol. 14, no. 5, pp. 2954–3009, 2021, doi: 10.1039/d1ee00247c.

[27] H. D. Chul, R. Vinodh, C. V. V. Muralee Gopi, C. Deviprasath, H. J. Kim, and M. Yi, “Effect of the cobalt and zinc ratio on the preparation of zeolitic imidazole frameworks (ZIFs): Synthesis, characterization and supercapacitor applications,” *Dalt. Trans.*, vol. 48, no. 39, pp. 14808–14819, 2019, doi: 10.1039/c9dt03306h.

[28] D. Lv *et al.*, “Efficient Mechanochemical Synthesis of MOF-5 for Linear Alkanes Adsorption,” *J. Chem. Eng. Data*, vol. 62, no. 7, pp. 2030–2036, 2017, doi: 10.1021/acs.jced.7b00049.

[29] D. Esken, S. Turner, O. I. Lebedev, G. Van Tendeloo, and R. A. Fischer, “Au@ZIFs: Stabilization and encapsulation of cavity-size matching gold clusters inside functionalized zeolite imidazolate frameworks, ZIFs,” *Chem. Mater.*, vol. 22, no. 23, pp. 6393–6401, 2010, doi: 10.1021/cm102529c.

[30] L. Chang, D. Cheng, L. Sementa, and A. Fortunelli, “Hydrogen evolution reaction (HER) on Au@Ag ultrananoclusters as electro-catalysts,” *Nanoscale*, vol. 10, no. 37, pp. 17730–17737, 2018, doi: 10.1039/c8nr06105j.

[31] T. Reier, M. Oezaslan, and P. Strasser, “Electrocatalytic oxygen evolution reaction (OER) on Ru, Ir, and pt catalysts: A comparative study of nanoparticles and bulk materials,” *ACS Catal.*, vol. 2, no. 8, pp. 1765–1772, 2012, doi: 10.1021/cs3003098.

[32] B. D. Zdravkov, J. J. Čermák, M. Šefara, and J. Janků, “Pore classification in the characterization of porous materials: A perspective,” *Cent. Eur. J. Chem.*, vol. 5, no. 2, pp. 385–395, 2007, doi: 10.2478/s11532-007-0017-9.

[33] V. Chaudhary and S. Sharma, “An overview of ordered mesoporous material SBA-15: synthesis, functionalization and application in oxidation reactions,” *J. Porous Mater.*, vol. 24, no. 3, pp. 741–749, 2017, doi: 10.1007/s10934-016-0311-z.

[34] M. L. Foo, R. Matsuda, and S. Kitagawa, “Functional hybrid porous coordination

polymers," *Chem. Mater.*, vol. 26, no. 1, pp. 310–322, 2014, doi: 10.1021/cm402136z.

[35] T. A. Goetjen *et al.*, "Metal-organic framework (MOF) materials as polymerization catalysts: A review and recent advances," *Chem. Commun.*, vol. 56, no. 72, pp. 10409–10418, 2020, doi: 10.1039/d0cc03790g.

[36] H. C. Zhou, J. R. Long, and O. M. Yaghi, "Introduction to metal-organic frameworks," *Chem. Rev.*, vol. 112, no. 2, pp. 673–674, 2012, doi: 10.1021/cr300014x.

[37] N. C. Burtch, H. Jasuja, and K. S. Walton, "Water stability and adsorption in metal-organic frameworks," *Chem. Rev.*, vol. 114, no. 20, pp. 10575–10612, 2014, doi: 10.1021/cr5002589.

[38] X. F. Lu, B. Y. Xia, S. Zang, and X. W. (David) Lou, "Metal–Organic Frameworks Based Electrocatalysts for the Oxygen Reduction Reaction," *Angew. Chemie*, vol. 132, no. 12, pp. 4662–4678, 2020, doi: 10.1002/ange.201910309.

[39] H. J. Buser, A. Ludi, D. Schwarzenbach, and W. Petter, "The Crystal Structure of Prussian Blue: Fe4[Fe(CN)6]3·xH2O," *Inorg. Chem.*, vol. 16, no. 11, pp. 2704–2710, 1977, doi: 10.1021/ic50177a008.

[40] B. F. Hoskins and R. Robson, "Design and Construction of a New Class of Scaffolding-like Materials Comprising Infinite Polymeric Frameworks of 3D-Linked Molecular Rods. A Reappraisal of the Zn(CN)2 and Cd(CN)2 Structures and the Synthesis and Structure of the Diamond-Related Framework," *J. Am. Chem. Soc.*, vol. 112, no. 4, pp. 1546–1554, 1990, doi: 10.1021/ja00160a038.

[41] B. Robert and E. B. Brown, "No 主観的健康感を中心とした在宅高齢者における 健康関連指標に関する共分散構造分析Title," no. 1, pp. 1–14, 2004.

[42] E. V. Perez, C. Karunaweera, I. H. Musselman, K. J. Balkus, and J. P. Ferraris, "Origins and evolution of inorganic-based and MOF-based mixed-matrix membranes for gas separations," *Processes*, vol. 4, no. 3, 2016, doi: 10.3390/pr4030032.

[43] K. K. Gangu, S. Maddila, S. B. Mukkamala, and S. B. Jonnalagadda, “A review on contemporary Metal-Organic Framework materials,” *Inorganica Chim. Acta*, vol. 446, pp. 61–74, 2016, doi: 10.1016/j.ica.2016.02.062.

[44] O. K. Farha *et al.*, “Metal-organic framework materials with ultrahigh surface areas: Is the sky the limit?,” *J. Am. Chem. Soc.*, vol. 134, no. 36, pp. 15016–15021, 2012, doi: 10.1021/ja3055639.

[45] B. Chen, Z. Yang, Y. Zhu, and Y. Xia, “Zeolitic imidazolate framework materials: Recent progress in synthesis and applications,” *J. Mater. Chem. A*, vol. 2, no. 40, pp. 16811–16831, 2014, doi: 10.1039/c4ta02984d.

[46] S. Bhattacharjee, M. S. Jang, H. J. Kwon, and W. S. Ahn, “Zeolitic Imidazolate Frameworks: Synthesis, Functionalization, and Catalytic/Adsorption Applications,” *Catal. Surv. from Asia*, vol. 18, no. 4, pp. 101–127, 2014, doi: 10.1007/s10563-014-9169-8.

[47] S. D. Taherzade, J. Soleimannejad, and A. Tarlani, “Application of metal-organic framework Nano-MIL-100(Fe) for sustainable release of doxycycline and tetracycline,” *Nanomaterials*, vol. 7, no. 8, 2017, doi: 10.3390/nano7080215.

[48] X. Wang *et al.*, “MOFBOTS: Metal–Organic-Framework-Based Biomedical Microrobots,” *Adv. Mater.*, vol. 31, no. 27, 2019, doi: 10.1002/adma.201901592.

[49] V. Chernikova, O. Yassine, O. Shekhah, M. Eddaoudi, and K. N. Salama, “Highly sensitive and selective SO2 MOF sensor: The integration of MFM-300 MOF as a sensitive layer on a capacitive interdigitated electrode,” *J. Mater. Chem. A*, vol. 6, no. 14, pp. 5550–5554, 2018, doi: 10.1039/c7ta10538j.

[50] T. D. Bennett *et al.*, “Melt-Quenched Glasses of Metal-Organic Frameworks,” *J. Am. Chem. Soc.*, vol. 138, no. 10, pp. 3484–3492, 2016, doi: 10.1021/jacs.5b13220.

[51] S. Kouser, A. Hezam, M. J. N. Khadri, and S. A. Khanum, “A review on zeolite imidazole frameworks: synthesis, properties, and applications,” *J. Porous Mater.*, vol. 29, no. 3, pp. 663–681, 2022, doi: 10.1007/s10934-021-01184-z.

[52] T. D. Bennett *et al.*, “Structure and properties of an amorphous metal-organic framework,” *Phys. Rev. Lett.*, vol. 104, no. 11, 2010, doi: 10.1103/PhysRevLett.104.115503.

[53] L. V. Sineva, E. Y. Asalieva, and V. Z. Mordkovich, “Role of zeolite in the synthesis of liquid hydrocarbons from CO and H2 on a composite cobalt catalyst,” *Catal. Ind.*, vol. 7, no. 4, pp. 245–252, 2015, doi: 10.1134/S2070050415040145.

[54] J. E. Naber, K. P. de Jong, W. H. J. Stork, H. P. C. E. Kuipers, and M. F. M. Post, “Industrial applications of zeolite catalysis,” *Stud. Surf. Sci. Catal.*, vol. 84, no. C, pp. 2197–2219, 1994, doi: 10.1016/S0167-2991(08)63783-0.

[55] S. Tedds, A. Walton, D. P. Broom, and D. Book, “Characterisation of porous hydrogen storage materials: Carbons, zeolites, MOFs and PIMs,” *Faraday Discuss.*, vol. 151, pp. 75–94, 2011, doi: 10.1039/c0fd00022a.

[56] Y. Sun, Y. Li, and J. C. Tan, “Liquid Intrusion into Zeolitic Imidazolate Framework-7 Nanocrystals: Exposing the Roles of Phase Transition and Gate Opening to Enable Energy Absorption Applications,” *ACS Appl. Mater. Interfaces*, vol. 10, no. 48, pp. 41831–41838, 2018, doi: 10.1021/acsami.8b16527.

[57] P. Zhao *et al.*, “Phase transitions in zeolitic imidazolate framework 7: The importance of framework flexibility and guest-induced instability,” *Chem. Mater.*, vol. 26, no. 5, pp. 1767–1769, 2014, doi: 10.1021/cm500407f.

[58] A. Ebrahimi and M. Mansournia, “Zeolitic imidazolate framework-7: Novel ammonia atmosphere-assisted synthesis, thermal and chemical durability, phase reversibility and potential as highly efficient nanophotocatalyst,” *Chem. Phys.*, vol. 511, pp. 33–45, 2018, doi: 10.1016/j.chemphys.2018.06.003.

[59] V. A. Polyakov, V. V. Butova, E. A. Erofeeva, A. A. Tereshchenko, and A. V. Soldatov, “Mw synthesis of zif-7. The effect of solvent on particle size and hydrogen sorption properties,” *Energies*, vol. 13, no. 23, 2020, doi: 10.3390/en13236306.

[60] M. Niknam Shahrak, M. Niknam Shahrak, A. Shahsavand, N. Khazeni, X. Wu,

and S. Deng, “Synthesis, gas adsorption and reliable pore size estimation of zeolitic imidazolate framework-7 using CO2 and water adsorption,” *Chinese J. Chem. Eng.*, vol. 25, no. 5, pp. 595–601, 2017, doi: 10.1016/j.cjche.2016.10.012.

[61] H. An *et al.*, “Facile Defect Engineering of Zeolitic Imidazolate Frameworks towards Enhanced C3H6/C3H8 Separation Performance,” *Adv. Funct. Mater.*, vol. 31, no. 47, 2021, doi: 10.1002/adfm.202105577.

[62] Y. Li and J. Yu, “Emerging applications of zeolites in catalysis, separation and host–guest assembly,” *Nat. Rev. Mater.*, vol. 6, no. 12, pp. 1156–1174, 2021, doi: 10.1038/s41578-021-00347-3.

[63] P. J. McHugh, A. D. Stergiou, and M. D. Symes, “Decoupled Electrochemical Water Splitting: From Fundamentals to Applications,” *Adv. Energy Mater.*, vol. 10, no. 44, 2020, doi: 10.1002/aenm.202002453.

[64] S. Zhao, D. W. Wang, R. Amal, and L. Dai, “Carbon-Based Metal-Free Catalysts for Key Reactions Involved in Energy Conversion and Storage,” *Adv. Mater.*, vol. 31, no. 9, 2019, doi: 10.1002/adma.201801526.

[65] K. Khan *et al.*, “Recent advances in two-dimensional materials and their nanocomposites in sustainable energy conversion applications,” *Nanoscale*, vol. 11, no. 45, pp. 21622–21678, 2019, doi: 10.1039/c9nr05919a.

[66] H. Bin Wu, B. Y. Xia, L. Yu, X. Y. Yu, and X. W. Lou, “Porous molybdenum carbide nano-octahedrons synthesized via confined carburization in metal-organic frameworks for efficient hydrogen production,” *Nat. Commun.*, vol. 6, 2015, doi: 10.1038/ncomms7512.

[67] A. K. M. Fazle Kibria and S. A. Tarafdar, “Electrochemical studies of a nickel-copper electrode for the oxygen evolution reaction (OER),” *Int. J. Hydrogen Energy*, vol. 27, no. 9, pp. 879–884, 2002, doi: 10.1016/S0360-3199(01)00185-9.

[68] C. N. Brodsky *et al.*, “In situ characterization of cofacial Co(IV) centers in Co4O4 cubane: Modeling the high-valent active site in oxygen-evolving catalysts,” *Proc. Natl. Acad. Sci. U. S. A.*, vol. 114, no. 15, pp. 3855–3860, 2017, doi:

10.1073/pnas.1701816114.

[69] A. J. Medford *et al.*, “From the Sabatier principle to a predictive theory of transition-metal heterogeneous catalysis,” *J. Catal.*, vol. 328, pp. 36–42, 2015, doi: 10.1016/j.jcat.2014.12.033.

[70] C. Vanhaverbeke, M. Cauwe, A. Stockman, M. Op de Beeck, and H. De Smet, “Comparison of copper electroplating, copper wet etching and linear sweep voltammetry as techniques to investigate the porosity of atomic layer deposited Al2O3,” *Thin Solid Films*, vol. 686, 2019, doi: 10.1016/j.tsf.2019.137424.

[71] F. Song *et al.*, “An Unconventional Iron Nickel Catalyst for the Oxygen Evolution Reaction,” *ACS Cent. Sci.*, vol. 5, no. 3, pp. 558–568, 2019, doi: 10.1021/acscentsci.9b00053.

[72] M. Rafiee, M. N. Mayer, B. T. Punchihewa, and M. R. Mumau, “Constant Potential and Constant Current Electrolysis: An Introduction and Comparison of Different Techniques for Organic Electrosynthesis,” *J. Org. Chem.*, vol. 86, no. 22, pp. 15866–15874, 2021, doi: 10.1021/acs.joc.1c01391.

[73] A. Munir *et al.*, “Ultrasmall Co@Co(OH)2 Nanoclusters Embedded in N-Enriched Mesoporous Carbon Networks as Efficient Electrocatalysts for Water Oxidation,” *ChemSusChem*, vol. 12, no. 23, pp. 5117–5125, 2019, doi: 10.1002/cssc.201902505.

[74] C. S. Cundy and P. A. Cox, “The hydrothermal synthesis of zeolites: Precursors, intermediates and reaction mechanism,” *Microporous Mesoporous Mater.*, vol. 82, no. 1–2, pp. 1–78, 2005, doi: 10.1016/j.micromeso.2005.02.016.

[75] S. Shen, L. Zhao, and L. Guo, “Morphology, structure and photocatalytic performance of ZnIn2S4 synthesized via a solvothermal/hydrothermal route in different solvents,” *J. Phys. Chem. Solids*, vol. 69, no. 10, pp. 2426–2432, 2008, doi: 10.1016/j.jpcs.2008.04.035.

[76] “Metal-Organic-Frameworks (MOFs) for Industrial Wastewater Treatment,” pp. 1–28, 2019, doi: 10.21741/9781644900291-1.

[77] M. Zhen, J. Yu, and S. Dai, “Preparation of inorganic materials using ionic liquids,” *Adv. Mater.*, vol. 22, no. 2, pp. 261–285, 2010, doi: 10.1002/adma.200900603.

[78] A. S. Manikandan, K. B. Renukadevi, K. Ravichandran, P. V. Rajkumar, and K. Boubaker, “Enhanced photocatalytic, antibacterial and magnetic properties of ZnO nanopowders through lattice compatible cobalt doping,” *J. Mater. Sci. Mater. Electron.*, vol. 27, no. 11, pp. 11890–11901, 2016, doi: 10.1007/s10854-016-5334-3.

[79] A. Martinez Joaristi, J. Juan-Alcañiz, P. Serra-Crespo, F. Kapteijn, and J. Gascon, “Electrochemical synthesis of some archetypical Zn 2+, Cu 2+, and Al 3+ metal organic frameworks,” *Cryst. Growth Des.*, vol. 12, no. 7, pp. 3489–3498, 2012, doi: 10.1021/cg300552w.

[80] Y. K. Hwang *et al.*, “Selective sulfoxidation of aryl sulfides by coordinatively unsaturated metal centers in chromium carboxylate MIL-101,” *Appl. Catal. A Gen.*, vol. 358, no. 2, pp. 249–253, 2009, doi: 10.1016/j.apcata.2009.02.018.

[81] J. S. Choi, W. J. Son, J. Kim, and W. S. Ahn, “Metal-organic framework MOF-5 prepared by microwave heating: Factors to be considered,” *Microporous Mesoporous Mater.*, vol. 116, no. 1–3, pp. 727–731, 2008, doi: 10.1016/j.micromeso.2008.04.033.

[82] T. Friščić *et al.*, “Real-time and in situ monitoring of mechanochemical milling reactions,” *Nat. Chem.*, vol. 5, no. 1, pp. 66–73, 2013, doi: 10.1038/nchem.1505.

[83] G. Zhan and H. C. Zeng, “Alternative synthetic approaches for metal-organic frameworks: transformation from solid matters,” *Chem. Commun.*, vol. 53, no. 1, pp. 72–81, 2017, doi: 10.1039/c6cc07094a.

[84] A. A. Bunaciu, E. gabriela Udriştioiu, and H. Y. Aboul-Enein, “X-Ray Diffraction: Instrumentation and Applications,” *Crit. Rev. Anal. Chem.*, vol. 45, no. 4, pp. 289–299, 2015, doi: 10.1080/10408347.2014.949616.

[85] R. Terzano, M. A. Denecke, G. Falkenberg, B. Miller, D. Paterson, and K.

Janssens, “Recent advances in analysis of trace elements in environmental samples by X-ray based techniques (IUPAC Technical Report),” *Pure Appl. Chem.*, vol. 91, no. 6, pp. 1029–1063, 2019, doi: 10.1515/pac-2018-0605.

[86] J. Liu, S. Wei, N. Li, L. Zhang, and X. Cui, “Delicate excavated trimetallic Prussian blue analogues for efficient oxygen evolution reactions,” *Electrochim. Acta*, vol. 299, pp. 575–581, 2019, doi: 10.1016/j.electacta.2019.01.003.

[87] J. Madejová, “FTIR techniques in clay mineral studies,” *Vib. Spectrosc.*, vol. 31, no. 1, pp. 1–10, 2003, doi: 10.1016/S0924-2031(02)00065-6.

[88] Y. R. Lee, M. S. Jang, H. Y. Cho, H. J. Kwon, S. Kim, and W. S. Ahn, “ZIF-8: A comparison of synthesis methods,” *Chem. Eng. J.*, vol. 271, pp. 276–280, 2015, doi: 10.1016/j.cej.2015.02.094.

[89] J. J. Ojeda and M. Dittrich, “Fourier transform infrared spectroscopy for molecular analysis of microbial cells,” *Methods Mol. Biol.*, vol. 881, pp. 187–211, 2012, doi: 10.1007/978-1-61779-827-6_8.

[90] C. Berthomieu and R. Hienerwadel, “Fourier transform infrared (FTIR) spectroscopy,” *Photosynth. Res.*, vol. 101, no. 2–3, pp. 157–170, 2009, doi: 10.1007/s11120-009-9439-x.

[91] W. Zhou, R. Apkarian, Z. L. Wang, and D. Joy, “Fundamentals of scanning electron microscopy (SEM),” *Scanning Microsc. Nanotechnol. Tech. Appl.*, pp. 1–40, 2007, doi: 10.1007/978-0-387-39620-0_1.

[92] K. Akhtar, S. A. Khan, S. B. Khan, and A. M. Asiri, “Scanning electron microscopy: Principle and applications in nanomaterials characterization,” *Handb. Mater. Charact.*, pp. 113–145, 2018, doi: 10.1007/978-3-319-92955-2_4.

[93] T. Buchner, T. Kiefer, W. Gaggl, L. Zelaya-Lainez, and J. Füssl, “Automated morphometrical characterization of material phases of fired clay bricks based on Scanning Electron Microscopy, Energy Dispersive X-ray Spectroscopy and Powder X-ray Diffraction,” *Constr. Build. Mater.*, vol. 288, 2021, doi: 10.1016/j.conbuildmat.2021.122909.

[94] M. D. Duca, C. L. Plosceanu, and T. Pop, “Effect of x-rays on poly(vinylidene fluoride) in x-ray photoelectron spectroscopy,” *J. Appl. Polym. Sci.*, vol. 67, no. 13, pp. 2125–2129, 1998, doi: 10.1002/(SICI)1097-4628(19980328)67:13<2125::AID-APP2>3.0.CO;2-G.

[95] S. Vepřek, D. L. Cocke, S. Kehl, and H. R. Oswald, “Mechanism of the deactivation of Hopcalite catalysts studied by XPS, ISS, and other techniques,” *J. Catal.*, vol. 100, no. 1, pp. 250–263, 1986, doi: 10.1016/0021-9517(86)90090-4.

[96] A. C. Ferrari and D. M. Basko, “Raman spectroscopy as a versatile tool for studying the properties of graphene,” *Nat. Nanotechnol.*, vol. 8, no. 4, pp. 235–246, 2013, doi: 10.1038/nnano.2013.46.

[97] Y. F. Huang *et al.*, “Surface-enhanced Raman spectroscopic study of p-aminothiophenol,” *Phys. Chem. Chem. Phys.*, vol. 14, no. 24, pp. 8485–8497, 2012, doi: 10.1039/c2cp40558j.

[98] R. R. Jones, D. C. Hooper, L. Zhang, D. Wolverson, and V. K. Valev, “Raman Techniques: Fundamentals and Frontiers,” *Nanoscale Res. Lett.*, vol. 14, no. 1, 2019, doi: 10.1186/s11671-019-3039-2.

[99] A. V. Vlasov *et al.*, “Raman scattering: From structural biology to medical applications,” *Crystals*, vol. 10, no. 1, 2020, doi: 10.3390/cryst10010038.

[100] M. C. Potcoava, G. L. Futia, J. Aughenbaugh, I. Schlaepfer, and E. A. Gibson, “Micro-Raman spectroscopy studies of changes in lipid composition in breast and prostate cancer cells treated with MPA and R1881 hormones,” *Biomed. Vib. Spectrosc. VI Adv. Res. Ind.*, vol. 8939, p. 89390I, 2014, doi: 10.1117/12.2040696.

[101] M. He, J. Yao, L. Li, K. Wang, F. Chen, and H. Wang, “Synthesis of zeolitic imidazolate framework-7 in a water/ethanol mixture and its ethanol-induced reversible phase transition,” *Chempluschem*, vol. 78, no. 10, pp. 1222–1225, 2013, doi: 10.1002/cplu.201300193.

[102] X. Wang *et al.*, “ZIF-7@carbon composites as multifunctional interlayer for rapid and durable Li-S performance,” *J. Energy Chem.*, vol. 57, pp. 19–27, 2021, doi:

10.1016/j.jechem.2020.09.019.

[103] Y. Li, F. Liang, H. Bux, W. Yang, and J. Caro, “Zeolitic imidazolate framework ZIF-7 based molecular sieve membrane for hydrogen separation,” *J. Memb. Sci.*, vol. 354, no. 1–2, pp. 48–54, 2010, doi: 10.1016/j.memsci.2010.02.074.

[104] R. Tatewaki *et al.*, “Control of ZIF-7-III aspect ratio using water-in-oil microemulsion,” *Colloids Surfaces A Physicochem. Eng. Asp.*, vol. 603, 2020, doi: 10.1016/j.colsurfa.2020.125157.

[105] N. Buğday, S. Altın, and S. Yaşar, “Porous carbon prepared by zeolitic imidazolate framework (ZIF-7-III) as the precursor for supercapacitor applications in different electrolytes,” *Int. J. Energy Res.*, vol. 46, no. 2, pp. 795–809, 2022, doi: 10.1002/er.7204.

[106] H. Luo *et al.*, “Removing nitrogen and phosphorus simultaneously in stormwater runoff using permeable asphalt pavement system with a zeolite-regulated reservoir,” *J. Water Reuse Desalin.*, vol. 10, no. 2, pp. 106–119, 2020, doi: 10.2166/wrd.2020.057.

[107] K. Kamali, S. Prasad, M. K. Sahoo, J. N. Behera, U. V. Waghmare, and C. Narayana, “Unusual CO2Adsorption in ZIF-7: Insight from Raman Spectroscopy and Computational Studies,” *Inorg. Chem.*, vol. 61, no. 30, pp. 11571–11580, 2022, doi: 10.1021/acs.inorgchem.2c00913.

[108] A. Malik and M. Nath, “Synthesis of Ag/ZIF-7 by immobilization of Ag nanoparticles onto ZIF-7 microcrystals: A heterogeneous catalyst for the reduction of nitroaromatic compounds and organic dyes,” *J. Environ. Chem. Eng.*, vol. 8, no. 6, 2020, doi: 10.1016/j.jece.2020.104547.

[109] S. Feng, X. Jia, J. Yang, Y. Li, S. Wang, and H. Song, “One-pot synthesis of core–shell ZIF-8@ZnO porous nanospheres with improved ethanol gas sensing,” *J. Mater. Sci. Mater. Electron.*, vol. 31, no. 24, pp. 22534–22545, 2020, doi: 10.1007/s10854-020-04764-y.

[110] N. Davoodian, A. Nakhaei Pour, M. Izadyar, A. Mohammadi, A. Salimi, and S. M.

Kamali Shahri, “Fischer–Tropsch synthesis using zeolitic imidazolate framework (ZIF-7 and ZIF-8)-supported cobalt catalysts,” *Appl. Organomet. Chem.*, vol. 34, no. 9, 2020, doi: 10.1002/aoc.5747.

[111] L. Longley, C. Calahoo, T. J. F. Southern, R. C. Evans, L. Wondraczek, and T. D. Bennett, “The reactivity of an inorganic glass melt with ZIF-8,” *Dalt. Trans.*, vol. 50, no. 10, pp. 3529–3535, 2021, doi: 10.1039/d1dt00152c.

[112] S. Zheng, D. Sun, L. Wu, S. Liu, and G. Liu, “Carbon fiber supported two-dimensional ZIF-7 interlayer for durable lithium-sulfur battery,” *J. Alloys Compd.*, vol. 870, 2021, doi: 10.1016/j.jallcom.2021.159412.

[113] S. S. Sankar, K. Karthick, K. Sangeetha, and S. Kundu, “In Situ Modified Nitrogen-Enriched ZIF-67 Incorporated ZIF-7 Nanofiber: An Unusual Electrocatalyst for Water Oxidation,” *Inorg. Chem.*, vol. 58, no. 20, pp. 13826–13835, 2019, doi: 10.1021/acs.inorgchem.9b01621.

[114] M. A. Asghar *et al.*, “Electrochemically Deposited Amorphous Cobalt-Nickel-Doped Copper Oxide as an Efficient Electrocatalyst toward Water Oxidation Reaction,” *ACS Omega*, vol. 6, no. 30, pp. 19419–19426, 2021, doi: 10.1021/acsomega.1c01251.

[115] A. Behera, “Metal-Organic Frameworks,” *Adv. Mater.*, pp. 637–666, 2022, doi: 10.1007/978-3-030-80359-9_19.